Impacts of Convective Activity over the Tibetan Plateau on Plateau Vortex, Southwest Vortex, and Downstream Precipitation

SHEN-MING FU,[a] ZI MAI,[b] JIAN-HUA SUN,[c] WAN-LI LI,[d] YANG DING,[e] AND YA-QIANG WANG[f]

[a] International Center for Climate and Environment Sciences, Institute of Atmospheric Physics,
Chinese Academy of Sciences, Beijing, China
[b] Key Laboratory of Cloud-Precipitation Physics and Severe Storms, Institute of Atmospheric Physics,
Chinese Academy of Sciences, and University of Chinese Academy of Sciences, Beijing, China
[c] Laboratory of Cloud–Precipitation Physics and Severe Storms, Institute of Atmospheric Physics,
Chinese Academy of Sciences, and State Key Laboratory of Severe Weather, Chinese
Academy of Meteorological Sciences, Beijing, China
[d] China Meteorological Administration Training Center, Beijing, China
[e] Shanghai Songjiang Meteorological Service, Shanghai, China
[f] State Key Laboratory of Severe Weather, and Key Laboratory of Atmospheric Chemistry of CMA,
Chinese Academy of Meteorological Sciences, Beijing, China

ABSTRACT

In summer, convective activity over the Tibetan Plateau (TP) is vigorous, with some of it moving eastward and vacating the plateau [defined as the eastward-moving type (EMT)]. Although the EMT only accounts for a small proportion, it is closely related to heavy precipitation east of the TP. This study investigates EMT impacts based on a series of composite semi-idealized simulations and piecewise potential vorticity (PV) inversion. The main results are as follows. (i) An EMT begins to affect downstream precipitation before it vacates the TP. A weaker EMT tends to cause the main downstream rainband to reduce in intensity and move southward. (ii) The EMT contributes to the formation of an eastward-moving plateau vortex (PLV) by enhancing convergence-induced stretching. Over the TP, the PLV mainly enhances/maintains the EMT, whereas during the vacating stage, the PLV dissipates (since convergence decreases rapidly when sensible heating from the TP reduces), which substantially reduces the intensity of the EMT. (iii) After PLV dissipation, a southwest vortex (SWV) forms around the Sichuan basin mainly due to convergence-induced stretching, convection-related tilting, and background transport. Piecewise PV inversion indicates that an EMT can directly contribute to SWV formation via lowering geopotential height and enhancing cyclonic wind perturbations around the Sichuan basin (even before its vacating stage), while neither of them governs the SWV formation. Sensitivity runs show that an EMT is not necessary for SWV formation, but can modify the SWV formation time and location, as well as its displacement, which significantly affects downstream precipitation.

1. Introduction

As the world's "third pole," the Tibetan Plateau (TP) (Table 1) has a mean height of ~4000 m and an area of ~2 500 000 km^2 (its principal range is 26°–40°N, 73°–104°E). Notable dynamic and thermodynamic effects associated with the TP occur throughout the year, and strongly affect the atmospheric circulation in East Asia and even worldwide (Ye and Gao 1979; Chen et al. 1985; Yanai et al. 1992; Wu and Zhang 1998; Xu 2001; Rangwala et al. 2009; Huang et al. 2010; Duan et al.

2013; Jiang et al. 2016; Zhao et al. 2018). In summer, under strong solar radiation (the instantaneous total radiation over the TP is ~23% larger than the solar constant), the TP serves as a major heat source to the atmosphere (its mean 500-hPa temperature of ~4.5 K is warmer than those in other regions at the same latitude) (Ye and Gao 1979; Lu et al. 1995; Zhang et al. 1998; Duan and Wu 2005; Xu et al. 2015). Moreover, favored by the moisture transport of the summer monsoon, the TP is also moister than other regions at the same altitude and latitude (Ye and Gao 1979; Xu et al. 2015; Zhao et al. 2018).

Because of the two abovementioned favorable conditions, convective activities over the TP are vigorous in

TABLE 1. Abbreviations used in this study.

Abbreviation	Original Terminology	Abbreviation	Original Terminology
TP	Tibetan Plateau	YRB	Yangtze River basin
EMT	Eastward-moving type	PLV	Plateau vortex
SWV	Southwest vortex	PV	Potential vorticity
T_{BB}	Temperature of blackbody	BST	Beijing standard time
MCE	Motion-caused effect	STR	Stretching
MTE	Mean transport effect	ETE	Eddy transport effect
TIL	Tilting	RES	Residue
PVU	Potential vorticity unit	MCS	Mesoscale convective system

summer (Jiang et al. 1996; Li et al. 2008; Hu et al. 2016, 2017). According to whether they vacate the TP, convective systems over the TP can be roughly classified into two groups (Jiang and Fan 2002; Li et al. 2008; Hu et al. 2017): (i) the dissipating over the TP type and (ii) the eastward-moving and vacating the TP type. For convenience, the latter type is defined as the eastward-moving type (EMT) in this study. Previous studies found that intense convective activities over the TP are usually closely related to a unique meso-α-scale vortex over the plateau—the plateau vortex (PLV) (Gao et al. 1981; Shen et al. 1986; Feng et al. 2014; Li et al. 2016). This type of vortex can induce precipitation over the TP (Gao et al. 1981; Wang 1987; Li et al. 2014), and when it moves to the eastern flank of the TP, it contributes to the enhancement of precipitation in downstream regions east of the TP[1] (He et al. 2009; Zhao and Wang 2010). Overall, only a small fraction of PLVs vacate the TP (Feng et al. 2014). This is consistent with the statistical result that EMTs account for the smallest percentage of all convective systems over the TP (Li et al. 2008; Hu et al. 2016). Most PLVs dissipate over the TP, particularly over the eastern flank (Feng et al. 2014; Li et al. 2014), but the mechanisms involved are not clearly understood.

The Yangtze River basin (YRB), located east of the TP, tends to experience heavy precipitation in summer (Tao 1980; Ding 1993; Zhao et al. 2004; Ni et al. 2017). Some of these events cause serious floods and waterlogging disasters that result in huge economic losses and serious numbers of casualties, such as the heavy rainfall events in 1931 and 1998 (Tao 1980; Ding 1993; Zhao and Fu 2007). For years, tremendous efforts have been made to understand the occurrence and evolution of heavy precipitation events over the YRB (Tao 1980; Chen and Wu 2000; Fujinami and Yasunari 2001; Xu 2001; Zhang et al. 2015; Wu et al. 2016; Yang et al. 2017). Among these studies, the impacts of EMTs on precipitation over the YRB is an important topic because, compared to other

types of convective systems generated over the TP, EMTs have a greater direct influence on downstream regions (Li et al. 2008; Fu et al. 2011; Hu et al. 2016). For instance, Jiang and Fan (2002) investigated the torrential precipitation events that occurred over the YRB in the summer of 1998 and found that some of these events can be traced back to EMTs. Qin et al. (2006) and Fu et al. (2010) analyzed heavy precipitation events related to southwest vortices (SWVs), a type of lee cyclone (Schär 1990; Wang and Chen 2002; McTaggart-Cowan et al. 2010). They suggested that EMTs can induce SWVs around the Sichuan basin after they move out of the TP, enhancing the precipitation to the east of the TP. Fu et al. (2011) analyzed EMTs in the meiyu season, and found that upper-tropospheric divergent centers associated with these systems can promote local ascending motion, and sometimes they can contribute to SWV formation in downstream regions after they vacate the TP.

Although previous studies have confirmed the importance of EMTs, the mechanisms underlying their effects on PLVs, SWVs, and downstream precipitation remain poorly understood. Therefore, the primary purpose of this study is to answer the following three scientific questions: What is the relationship between EMTs and PLVs? Why do PLVs tend to dissipate over the eastern flank of TP? How do EMTs affect the formation of SWVs and the precipitation in downstream regions east of the TP?

The remainder of the paper is structured as follows. Section 2 describes the data, model configuration, design of the semi-idealized simulations, and analysis methods. Section 3 provides a validation of the simulation and an overview of the event studied. Sections 4 and 5 show the main results relating to PLVs, SWVs, and EMTs. Finally, a discussion and conclusions are provided in section 6.

2. Data, model, and methods

a. Data

Climate Forecast System data, version 2 (Saha et al. 2014), at a 6-hourly temporal resolution and 0.5° × 0.5° spatial resolution, are used to generate the initial and boundary conditions for the semi-idealized simulations.

---

[1] In this study, the downstream regions mainly refer to the Yangtze River basin.

These data are also used to validate the simulated results. The $0.05° \times 0.05°$ satellite blackbody temperature (T_{BB}) data from *Himawari-8* (Bessho et al. 2016) are used to analyze the observed convective systems. Rain gauge–based 6-hourly cumulative precipitation data from the China Meteorological Administration are used to evaluate the precipitation produced by the semi-idealized simulation.

b. Model configuration

The multiscale processes relating to convective activity over the TP are simulated using a one-way, triple-nested (36, 12, and 4 km), convection-permitting configuration of the Advanced Research version of the WRF Model (Skamarock et al. 2008). The 30-s USGS topography data and MODIS land-use data are used in the simulation. The domains d01, d02, and d03 consist of 331×241, 541×331, and 1141×721 grid points, respectively (Fig. 1), respectively, with 51 levels in the vertical and a model top fixed at 50 hPa. The Yonsei University planetary boundary layer scheme (Noh et al. 2001), WRF single-moment 6-class microphysics scheme (Hong and Lim 2006), and Noah land surface model (Chen and Dudhia 2001) are used in all three domains. The Kain–Fritsch cumulus parameterization scheme (Kain 2004) is used in d01 and d02, and is switched off in d03. In this study, all analyses and calculations are based on the output from d03, except for Fig. 4, which uses the output from d01 to represent the background circulations.

c. Semi-idealized simulation design

As described in the introduction, EMTs are the research focus for this study. To understand this type of convective system from its common features, a semi-idealized composite simulation is designed and used as the control run in this study. Eight related events in the summer of 2016 (Fig. 2; Table 2) are used in the composite. These EMTs are first tracked using an objective tracking method (Li et al. 2012) on the T_{BB} data from the *Himawari-8* satellite (appendix A), and then validated manually (appendix B). Overall, four important common features are found among the eight events used in the composite: (i) all eight primary EMTs[2] are influenced by a PLV (appendix C) and/or a shortwave trough over the TP; (ii) the strong vacating stages[3] of
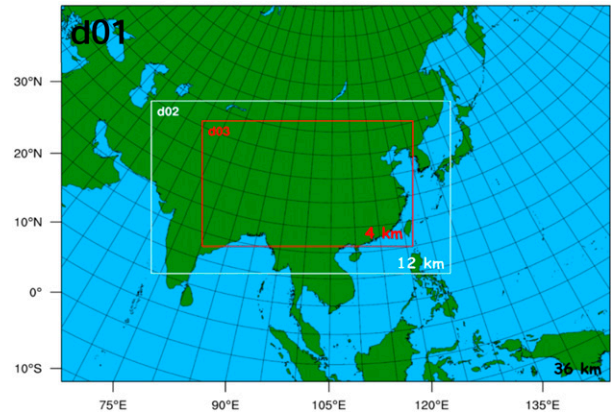

FIG. 1. Configuration of the one-way triply nested domains for the semi-idealized simulations.

these primary EMTs all begin in the afternoon (around 1200 UTC); (iii) all primary EMTs in these eight events contribute to the formation/enhancement of an SWV and/or low-level shear line east of the TP after they vacate the TP; and (iv) all primary EMTs induce heavy precipitation events east of the TP (Fig. 3; Table 2).

The initial and boundary conditions for the semi-idealized runs are designed as follows. If n represents the event number, then the value of a sample variable V at the time when the strong vacating stage of the primary EMT in event n begins is defined as $V_n(0)$. The time series [$V_n(-6)$, $V_n(-5)$, $V_n(-4)$, $V_n(-3)$, $V_n(-2)$, $V_n(-1)$, $V_n(0)$, $V_n(1)$, $V_n(2)$, $V_n(3)$, $V_n(4)$], with intervals of 6 h, then represents the period from 36 h before the start of the strong vacating stage in event n to 24 h after this point. For the eight events, the corresponding times are composited, equally weighted, in the Eulerian coordinate system. This results in an idealized 60-h time series, with 6-h intervals. The initial and boundary conditions for the semi-idealized run are produced by this ideal time series. Because $V_n(-6)$ is at 0000 UTC, the simulation is initiated at 0000 UTC, or 0800 Beijing Standard Time (BST). Correspondingly, the strong vacating stage starts at 1200 UTC. This is consistent with the diurnal variations of EMTs over the TP (Huang et al. 2010; Hu et al. 2016).

To answer the three scientific questions raised in the introduction, this study conducts four simulations as Table 3 shows, including a control run (CNTL), a run with no latent heating over the TP (NOLH), a run with latent heating within the Sichuan basin turned off (SBOF), and a run with no downward shortwave radiation at the surface of the TP (NOSW).

d. Piecewise potential vorticity inversion

Piecewise potential vorticity (PV) inversion (Davis and Emanuel 1991; Fu et al. 2014) is utilized in this study

---

[2] If an event has only one EMT, this EMT is the primary EMT. If an event has more than one EMT, the strongest EMT is defined as the primary EMT.

[3] Since the sizes of various EMTs are different, this study uses the moment when the center of a primary EMT begins to vacate the TP as the standard. This moment is defined as the start of the strong vacating stage, as around this time the relatively stronger section of the EMT also begins to vacate the TP.
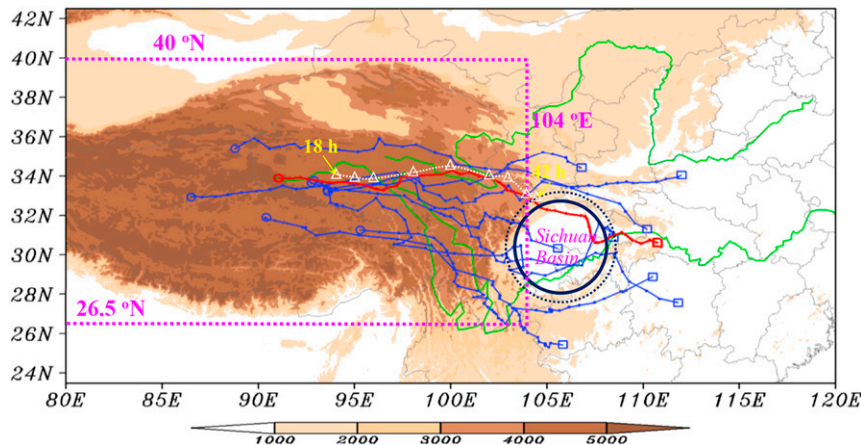
FIG. 2. The track of the CNTL-run-simulated PLV (white open triangles with dashed lines, where the first and last time of the vortex are marked with yellow numbers), tracks of the primary EMT of convective systems (blue solid lines) in the eight events used in the composite, the CNTL-run-simulated EMT track (red solid line), and terrain (shading; m), where the open circles mark the initial locations of the convective systems and the open rectangles show their dissipation locations. The solid dark blue circle marks the domain within which the SBOF run turned off only the latent heating. The ring between the solid and dashed dark blue circles shows the relaxation zone, where the latent heating was reduced from 100% to 0% linearly. The purple dashed lines illustrate the region used in the NOLH run.

to estimate the direct effects of convective activity. The PV used here is that defined by Ertel (1942), and the Charney balance equation (Charney 1955) is used in the calculation. As the PV budget equation documented by Koshyk and McFarlane (1996) shows, convection-related latent heating can produce positive PV anomalies. In this study, we isolate these positive anomalies that are mainly due to convective activity, originating from the TP, as follows: (i) vertically, the positive PV anomalies should be in the layer 500–200 hPa (500 hPa is close to the surface of the TP, and 200 hPa separates PV anomalies in the troposphere from those in the stratosphere); and (ii) horizontally, the positive PV anomalies should be located within the range 26.5°–40°N, 78°–108°E, which includes the TP and the regions into which EMTs can move; and (iii) all positive PV anomalies in (i) and (ii) are set to zero when the relative humidity is less than 75% (i.e., only latent-heating-generated PV anomalies are retained). These isolated anomalies are then inverted using piecewise PV inversion (Davis and Emanuel 1991). This produces their associated perturbation geopotential height and perturbation wind field. These perturbations are used to estimate the direct effects of convective activity originating from the TP.

e. Circulation budget

In this study, the circulation budget equation (Davis and Galarneau 2009; Fu and Sun 2012) is used to analyze the evolution of PLVs and SWVs:

$$\frac{\delta C}{\delta t} = \underbrace{-\overline{\eta}\tilde{\delta}A}_{\text{STR}} - \underbrace{\oint \eta' \overline{\mathbf{V}}_h \cdot \mathbf{n}\, dl}_{\text{MTE}} + \underbrace{\oint \omega \left(\mathbf{k} \times \frac{\partial \mathbf{V}_h}{\partial p} \right) \cdot \mathbf{n}\, dl}_{\text{TIL}}$$

$$- \underbrace{\oint \eta' \mathbf{V}'_h \cdot \mathbf{n}\, dl}_{\text{ETE}} + \underbrace{\mathbf{M}_h \cdot \nabla_h C}_{\text{MCE}} + \text{RES},$$

(1)

where η is the absolute vorticity, A is the system's area, and $\tilde{\delta}$ is the mean divergence within A. An overbar indicates an average around the perimeter of the system, and a prime denotes a perturbation from this mean. The vector $\mathbf{V}_h = u\mathbf{i} + v\mathbf{j}$ reprsents the wind, subscript h

TABLE 2. Start and end dates of the eight events used for the composite semi-idealized simulation and the maximum 6-h accumulated precipitation (over the YRB) associated with the eight primary EMTs.

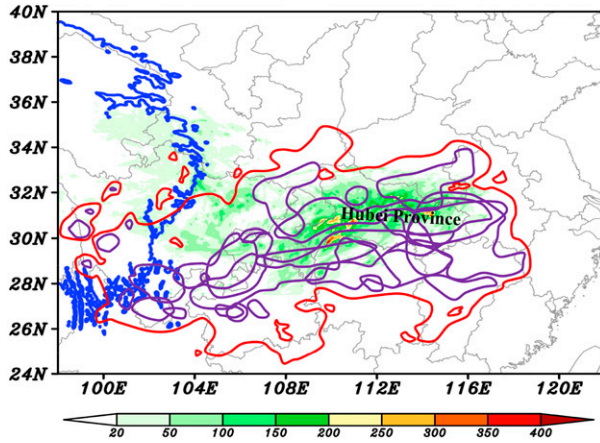| Event No.	Starting date	Ending date	Maximum 6-h accumulated precipitation (mm)
1	7 Jun 2016	8 Jun 2016	50
2	14 Jun 2016	15 Jun 2016	74
3	18 Jun 2016	19 Jun 2016	67
4	22 Jun 2016	23 Jun 2016	43
5	27 Jun 2016	28 Jun 2016	51
6	28 Jun 2016	30 Jun 2016	59
7	4 Jul 2016	5 Jul 2016	55
8	16 Jul 2016	18 Jul 2016	71

FIG. 3. The CNTL-run-simulated accumulated precipitation related to the EMT from the beginning to its exit of the TP (shading; mm), the corresponding accumulated precipitation above 50 mm related to the eight EMTs used for the composite (the thick purple solid lines outline the contour of 50-mm precipitation), and the mean value of 10 mm of the corresponding accumulated precipitation related to the eight EMTs used for the composite (thick red solid line). The thick blue line shows the terrain above 3000 m.

means the horizontal component, $\mathbf{n}$ is the unit vector normal to the boundary line of the system, ω is the vertical velocity in the p coordinate, and $\mathbf{i}$, $\mathbf{j}$, and $\mathbf{k}$ are unit vectors pointing to the east, north, and zenith, respectively. The vector $\mathbf{M}_h$ represents the horizontal velocity of the system, $\nabla_h = [(\partial/\partial x)\mathbf{i}] + [(\partial/\partial y)\mathbf{j}]$, and $C = \oint \mathbf{V}_h \cdot dl$ is the circulation along the system's boundary line. The operator $\delta/\delta t = (\partial/\partial t) + \mathbf{M}_h \cdot \nabla_h$ represents the quasi-Lagrangian variation.

The term $-\overline{\eta}\tilde{\delta}A$ stands for the stretching effect (STR) associated with the system's divergence; $-\oint \eta' \overline{\mathbf{V}_h} \cdot \mathbf{n} \, dl$ denotes the mean transport (MTE) of the perturbation absolute vorticity; $\oint \omega(\mathbf{k} \times \partial \mathbf{V}_h/\partial p) \cdot \mathbf{n} \, dl$ represents the tilting (TIL) of the total flow; $-\oint \eta' \mathbf{V}_h' \cdot \mathbf{n} \, dl$ denotes the eddy transport effects (ETE) of the perturbation absolute vorticity; $\mathbf{M}_h \cdot \nabla_h C$ denotes the motion effect (MCE) due to the movement of the system; and RES

represents the effects due to friction, subgrid processes, and calculation uncertainties (Table 1).

3. Simulation validation and overview of the case study

a. Validation of CNTL

A comparison between the left- and right-hand columns of Fig. 4 shows that the simulation reproduces the key features of the background circulation systems reasonably well, particularly for the 500-hPa eastward-moving shortwave trough and the diurnal variation of the temperature field over the TP, as well as the location and distribution of the 200-hPa upper-level jet. The methods described in appendixes A and B are used for tracking the simulated primary EMT. From Fig. 2, it is clear that the track of the simulated primary EMT is generally similar to the trajectory clustering result of the eight primary EMTs: (i) the formation location of the simulated primary EMT is near the mean initiation location of the eight EMTs and (ii) its dissipation location is near the mean latitude of the eight dissipation locations, with its longitude ~2° west (5° east) of the largest (smallest) longitude of the eight EMTs. The simulated strong vacating stage begins at $t = \sim$33 h, which is ~3 h earlier than the composite. Before $t = 33$ h, the simulated primary EMT mainly moves eastward, whereas after that it mainly changes to moving southeastward. This is consistent with the trajectory clustering result for the eight EMTs (not shown). As Fig. 3 shows, the simulation produces a heavy rainband, which is mainly located over the YRB and stretches from southwest to northeast. The precipitation simulation is consistent with the salient features of the eight events, in terms of heavy precipitation regions (thick purple solid lines in Fig. 3) and distribution of the main rainband (thick red solid lines in Fig. 3). The most significant differences appear over the eastern flank of the TP, where the simulated precipitation is at a higher latitude than that of the mean precipitation of the eight events. This is

TABLE 3. List of the semi-idealized simulations in this study and their configurations.

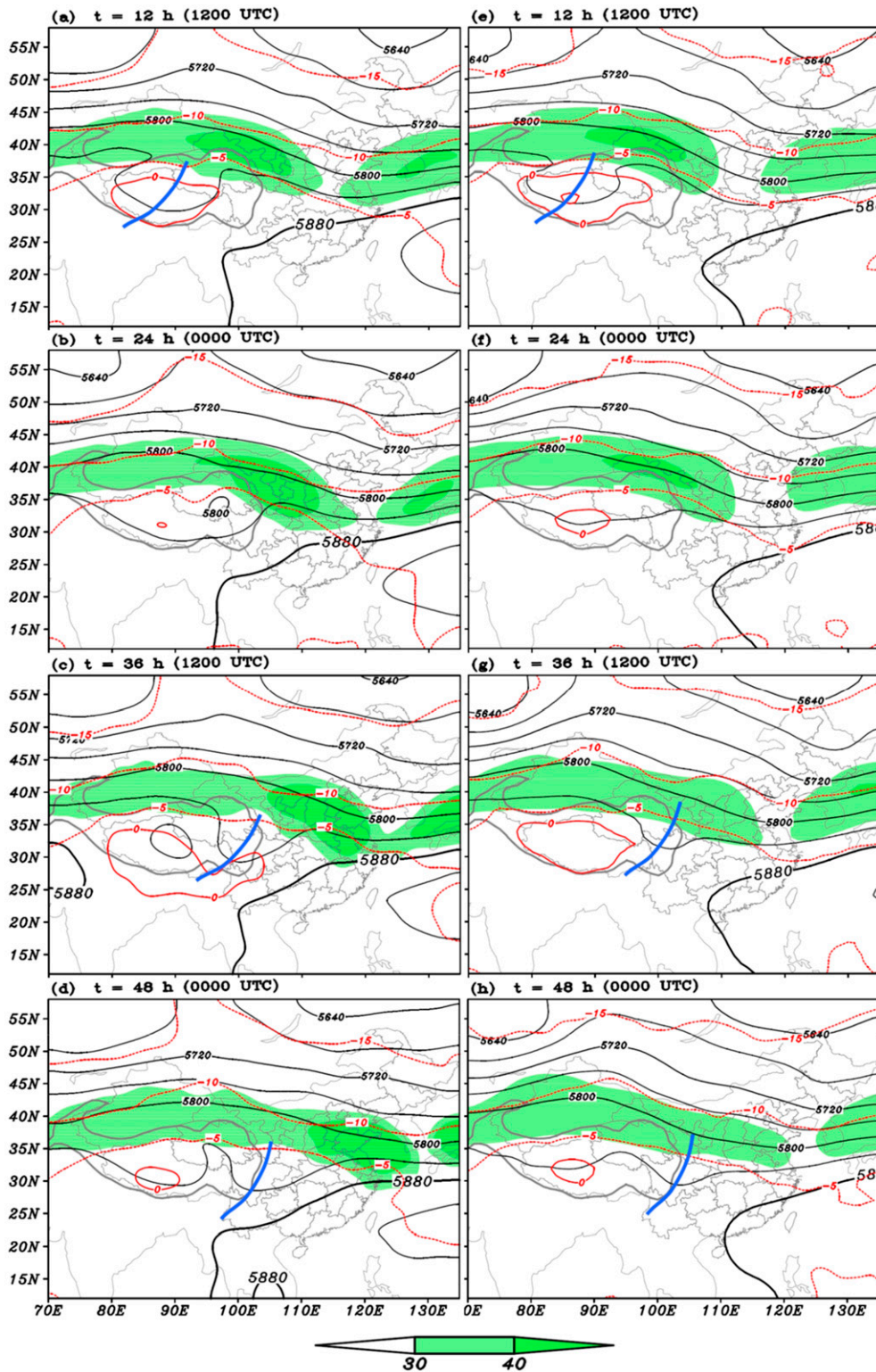| Expt	Objectives	Configurations
CNTL	To produce the main features associated with the EMT of convective systems from a commonness viewpoint	As shown in sections 2b and 2c
NOLH	Sensitivity to the convective activities related latent heating over the TP	Turn off only the latent heating within 26.5°–40°N, 78°–104°E (Fig. 2)
SBOF	Sensitivity to the convective activities related latent heating within the Sichuan basin	Turn off only the latent heating within the Sichuan basin (a circle centered at 30.3°N, 105.8°E, with a radius of 2.5°) (Fig. 2)
NOSW	Sensitivity to the downward shortwave flux related sensible heating over the TP	Fix the local time at midnight within 26.5°–40°N, 78°–104°E (Fig. 2)

FIG. 4. (a)–(d) The CNTL simulation results and (e)–(h) the corresponding composites, where the black solid line is the 500-hPa geopotential height (gpm), the red line is the 500-hPa temperature (°C), the shading is the 200-hPa wind speed above 30 m s^{-1} (m s^{-1}), the thick gray solid line marks the terrain higher than 3000 m, and the thick blue solid line marks the 500-hPa shortwave trough.

because the simulated EMT is at a higher latitude than that of the trajectory clustering of the eight EMTs over the eastern TP (not shown). In the lower troposphere, the simulation produces an SWV around the Sichuan basin after the EMT vacates the TP; this is a common feature for the eight events used in the composite (not shown).

Overall, as mentioned above, although there are some differences between the simulation and observations, CNTL reproduces the salient features of the eight events reasonably well and is therefore representative of this type of event.

b. Overview of the CNTL event

At $t = \sim 12$ h (i.e., when the CNTL simulation has been run for ~ 12 h), the CNTL-simulated primary EMT forms at around 34°N, 90.5°E (Fig. 5a), within the central region of a 500-hPa trough and a warm center over the TP (Fig. 4a), and on the right-hand side of the entry region of the 200-hPa upper-level jet (where its associated secondary circulation promotes ascending motion). Supported by condensational heating, a mesoscale vortex forms 6 h later (Fig. 6a), around which positive PV appears below 250 hPa (Fig. 7a). According to the definition given in appendix C, this mesoscale vortex is a PLV. It enhances the primary EMT, as indicated by the composite reflectivity (Fig. 5b), vorticity, PV, and ascending motion (Fig. 7a).

From $t = 18$ to 33 h, steered by the westerly wind, the primary EMT moves eastward. During this period, the EMT is enhanced by the PLV (Figs. 6a–f), which promotes ascending motion through the positive feedback among latent heating, convergence, and ascending motion (Raymond and Jiang 1990). The PLV is embedded within the central region of a 500-hPa shortwave trough over the TP (Figs. 5b–f), which also moves eastward. Corresponding to the above processes, the regions of vigorous convection over the TP move eastward, from west of 96°E to east of the TP (Figs. 7a–d). By $t = 30$ h, a positive PV and cyclonic vorticity center appears at around 101°E, above which a strong ascending-motion center forms at around 350 hPa (Fig. 7c). These features are consistent with the strengthening of the PLV (Fig. 6e).

The strong vacating stage starts at $t = \sim 33$ h, when the PLV begins to move out of the TP (Fig. 6f), and ends at around $t = 45$ h, when the PLV dissipates and the primary EMT is located almost entirely to the east of the TP (Fig. 6j). This stage can be further divided into two periods: period A is an earlier period (from $t = 33$ to 36 h), when the PLV enhances gradually (as Figs. 5g and 7e show, the maximum intensity of the PLV appears at around $t = 36$ h) and the primary EMT retains its strength (Figs. 6f,g); and (b) period B is a later period (from $t = 36$ to 45 h), when the cyclonic vorticity, PV,

and ascending motion over the eastern flank of the TP (100°–104°E) decrease quickly, consistent with the weakening of the PLV and the primary EMT (Figs. 6h–j). In contrast to the weakening processes over the eastern flank of the TP, new cyclonic vorticity, PV (104°–108°E), and ascending motion (106°–111°E) intensify rapidly east of the TP (Figs. 7e–h) during the later period. These intensifying features are mainly due to the enhancement of a lower-level shear line and the formation of an SWV (Figs. 8g–j). Both are located ahead of the 500-hPa shortwave trough that has moved out of the TP (Figs. 5g–j). Overall, during the lifespan of the PLV, the EMT and the vortex are coupled together and follow similar tracks (Fig. 2). The EMT has a larger area than the PLV, with strong reflectivity mainly located around the eastern section of the vortex (Fig. 6).

The primary EMT clearly induces rainfall over the eastern flank of the TP. The Sichuan basin and Hubei Province (109°–116°E) (Fig. 3) also experience precipitation that is related to the EMT. Overall, precipitation increases to the east (i.e., light precipitation over the TP, moderate precipitation within the Sichuan basin, and heavy precipitation around Hubei Province). This distribution is consistent with the distribution of lower-level moisture (not shown).

4. Evolution of the PLV and formation of the SWV

The CNTL-simulated primary EMT, which is associated with an eastward-moving shortwave trough over the TP (Fig. 5), forms at around $t = 12$ h and lasts for the rest of the simulation period (i.e., until $t = 60$ h). During its lifetime, its key structure changes after vacating the TP: over the TP (from $t = 18$ to 42 h), a PLV is within the primary EMT, whereas east of the TP (from $t = 42$ to 60 h), an SWV is within it. Both the PLV and SWV are favorable for maintaining the strong intensity of the EMT. The vortices are discussed in detail in this Section.

a. Evolution of the PLV

To investigate the evolutionary mechanisms of the PLV, Eq. (1) is used. The calculation is conducted within a 5° × 5° box (see Fig. 6). This vortex-following box is defined as the key region of the PLV. It is determined by the average size of the PLV, and satisfies two main conditions: (i) it covers the main body of the PLV during its whole lifetime; and (ii) calculation results based on it are insensitive to relatively small changes (±0.5°) to its boundaries. Tests indicate that, overall, Eq. (1) is reasonably balanced without consideration of the friction-related term RES (not shown). This means that RES can be neglected for this event.
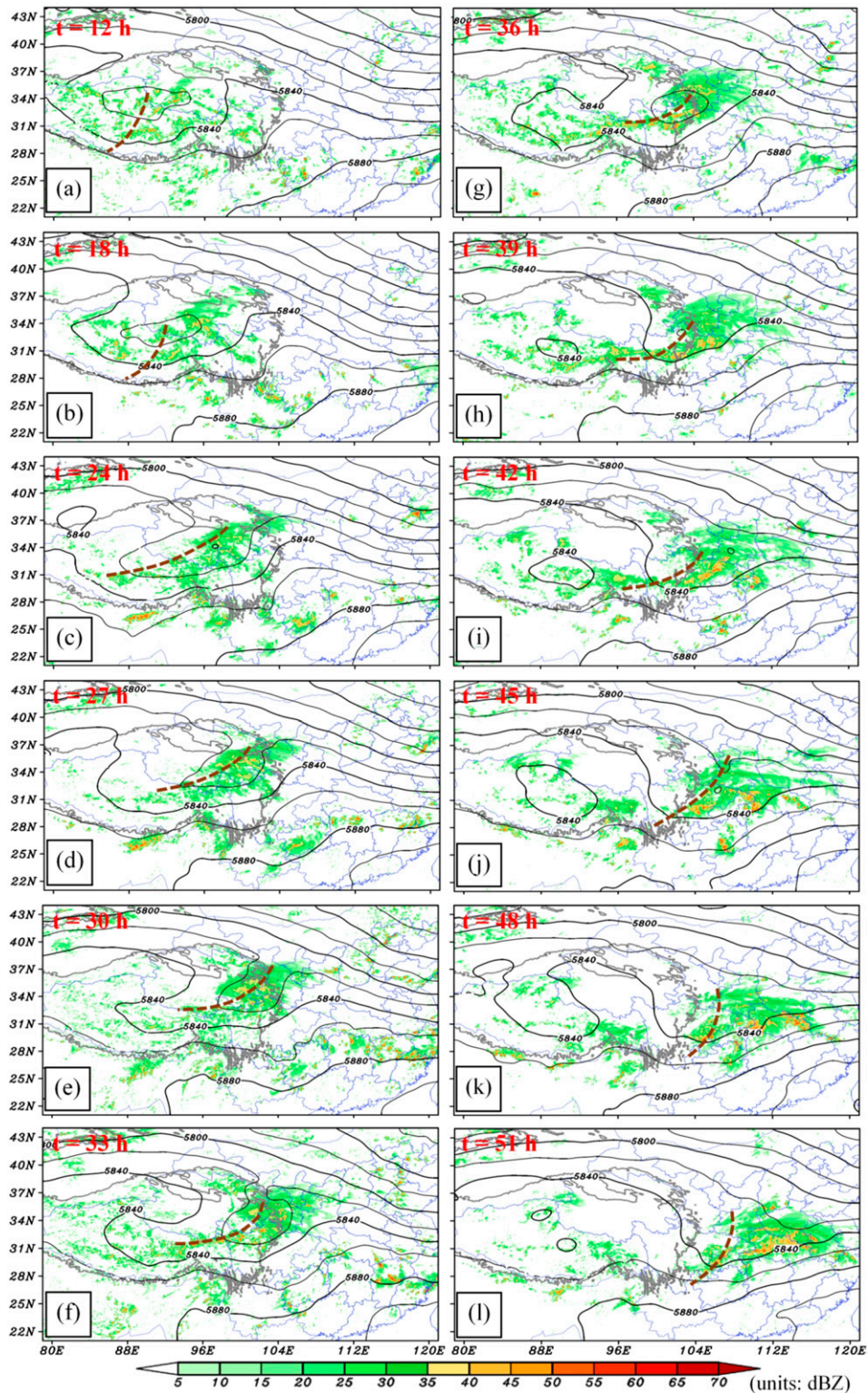
FIG. 5. The composite reflectivity (shading; dBZ) and the 500-hPa geopotential height (black solid; gpm) in the CNTL run, where the brown dashed lines are the trough lines and the thick gray line shows the terrain above 3000 m.
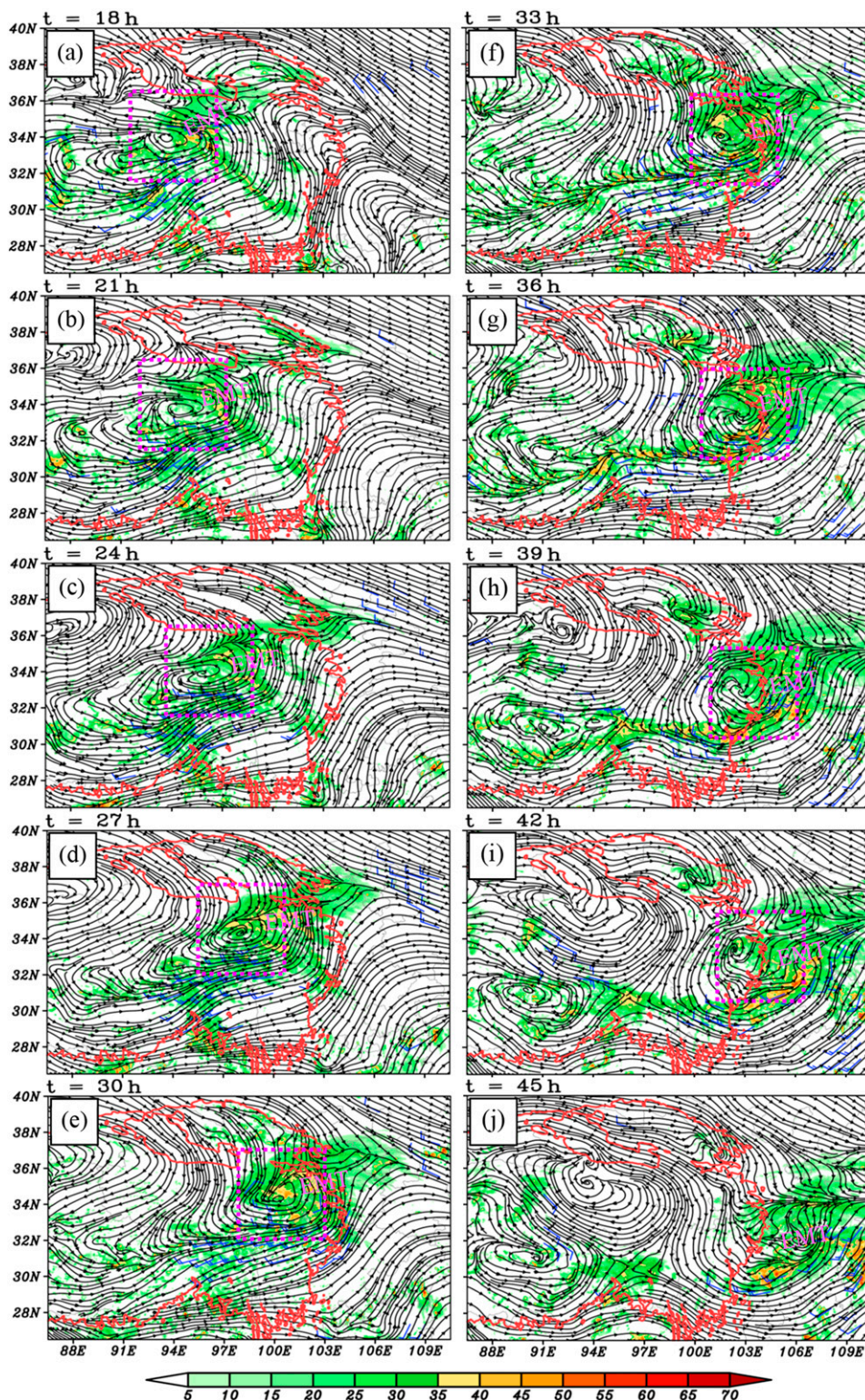
FIG. 6. The composite reflectivity (shading; dB*Z*), streamline field and wind above 12 m s^{-1} at 500-hPa (blue wind barbs; a full barb is 10 m s^{-1}) in the CNTL run, where the thick red solid line marks terrain at 3000 m, the dashed purple boxes are the key regions of the PLV, and the purple "EMT" marks the primary EMT in the simulation.
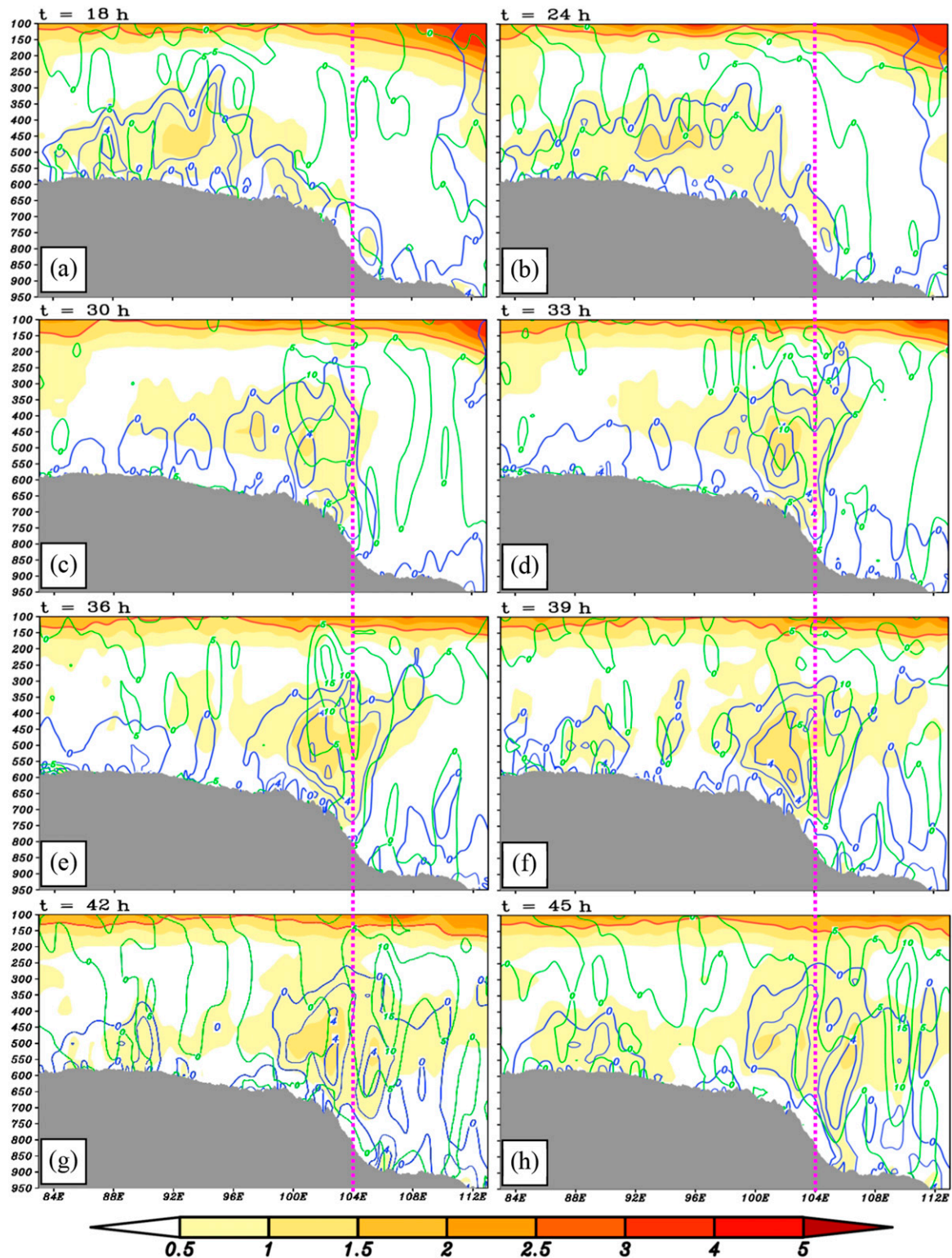
FIG. 7. The meridional mean (30°–37°N) PV (shading; PVU; 1 PVU = 10^{-6} K kg^{-1} m^2 s^{-1}), relative vorticity (blue solid lines; 10^{-5} s^{-1}), and vertical motions (green lines; cm s^{-1}), in the CNTL run, where the thick red solid line show the 1.5-PVU contour, the gray shading shows the meridional mean terrain, and the purple dashed line shows the eastern boundary of the TP (104°E).
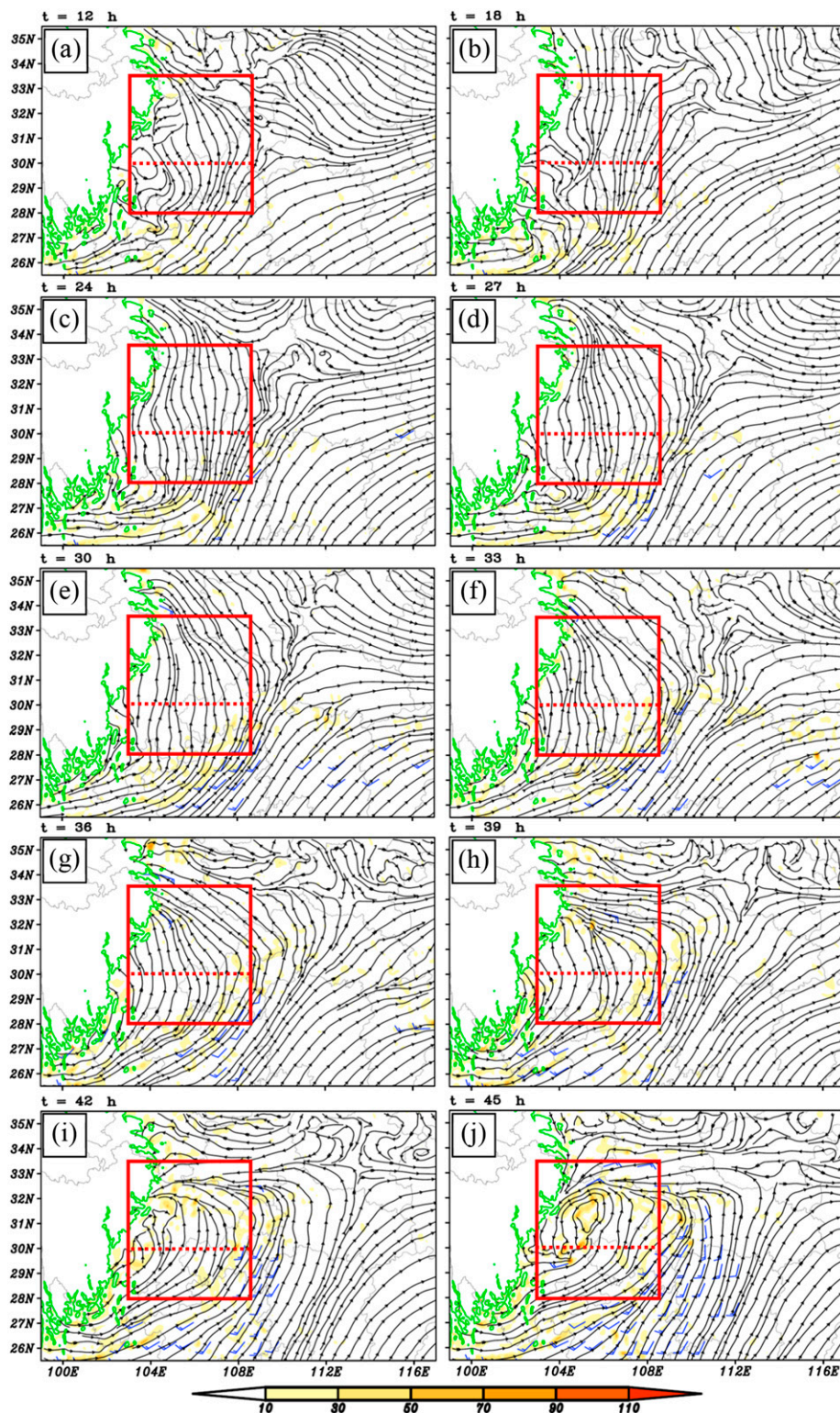
FIG. 8. The CNTL-run-simulated 700-hPa streamline field, vorticity (shading; $10^{-5}\,\mathrm{s}^{-1}$), and wind above $12\,\mathrm{m\,s}^{-1}$ (blue wind barbs; a full barb is $10\,\mathrm{m\,s}^{-1}$), where the thick green solid line marks terrain at 3000 m, and the red box is the key area of the SWV, with the dashed red line showing 30°N.

As Fig. 9a shows, from $t = 12$ to $18\,h$ (before the formation of the PLV), the key region (box in Fig. 6a) is dominated by convergence and ascending motion. Cyclonic circulation/vorticity within the key region increases gradually around $500\,hPa$ (525–$475\,hPa$), corresponding to the formation process[4] of the PLV. Convergence-related STR governs the PLV formation (Fig. 9b), which is consistent with findings in previous studies (e.g., Shen et al. 1986; Wang 1987; Zhao et al. 2004). In contrast, the eddy transport (i.e., ETE) acts as the most detrimental factor to PLV formation (Fig. 9e), by causing a net export of cyclonic vorticity from the key region.

The period from $t = 18$ to $36\,h$ is the developing stage of the PLV (section 3b). This is confirmed by the rapid enhancement of cyclonic vorticity around $500\,hPa$ (525–$475\,hPa$) within the key region (Fig. 9a). During this stage, convergence associated with the PLV first maximizes in intensity (around $t = 30\,h$), then ascending motion reaches its maximum (around $t = 33\,h$), and finally cyclonic vorticity peaks (around $t = 36\,h$). The calculation indicates that the convergence-related STR term governs the enhancement of the cyclonic circulation of the PLV (Fig. 9b). The strong convergence around $500\,hPa$ is a result of positive feedback among convergence, ascending motion, and latent heating (Raymond and Jiang 1990). In addition, the movement of the PLV (i.e., MCE) also favors cyclonic circulation (Fig. 9f), as the vortex mainly moves from areas of lower cyclonic vorticity to regions of higher cyclonic vorticity (Fu and Sun 2012; Fu et al. 2015a). On the contrary, tilting (i.e., TIL) is the most detrimental factor to PLV development, as it mainly turns vertical vorticity into horizontal vorticity. In addition, the transports by mean and eddy flow (i.e., MTE and ETE) (Figs. 9c,e) mainly cause a net export of cyclonic vorticity from the key region, which also decelerates the intensification of the vortex.

From $t = 36$ to $45\,h$, the PLV weakens rapidly (Figs. 6g,h), as reflected by the rapid decline in the cyclonic vorticity/circulation around $500\,hPa$ (525–$475\,hPa$) within the key region (Fig. 9a). Tilting still acts to reduce vertical vorticity, which is detrimental to sustaining the PLV (Fig. 9d). Transport of vorticity by eddy flow mainly causes an export of cyclonic vorticity from the key region, which also contributes to PLV dissipation (Fig. 9e). In contrast, the transport by mean flow (i.e., MTE) is the most important factor resisting the

dissipation (Fig. 9c), as it mainly transports cyclonic vorticity into the key region (not shown). Impacts of the PLV displacement (i.e., MCE) change during this period, as the horizontal distribution of vorticity is inhomogeneous (not shown), but overall it is detrimental to prolonging the vortex lifetime (Fig. 9f). Following the variation of divergence associated with the PLV (Fig. 9a), STR first contributes to PLV dissipation due to divergence, and then favors its persistence due to convergence (Fig. 9b). Its overall effect on the persistence of the vortex, however, is favorable.

Comparing PLV-related budget terms in Eq. (1), it is clear that the term showing the most significant change between the developing stage of the PLV (from $t = 18$ to $36\,h$) and its dissipation stage (from $t = 36$ to $45\,h$) is STR (Fig. 9b). Although the eddy transport and tilting directly enhance the dissipation process of the PLV (Figs. 9d,e), these two terms mainly retain their negative effects (each term's mean effect during both the developing and dissipation stages is negative), and do not greatly change during the developing and dissipation stages. Therefore, it can be concluded that the significant weakening of convergence associated with the PLV results in a sharp decrease in STR (Fig. 9b). This is the reason for the changes from favorable conditions for PLV development/maintenance to unfavorable conditions [i.e., the total effect (gray lines in Fig. 9b) of the terms on the right-hand side of Eq. (1) changes from positive to negative]. The sharp weakening of the convergence associated with the PLV is mainly due to the vortex moving out of the TP (section 5b).

b. SWV formation

The formation of the SWV is investigated by solving Eq. (1) within a $5.5° \times 5.5°$ box, which is defined as the key area for the SWV. This area is fixed as shown in Fig. 8. It also satisfies two main conditions: (i) it covers the main body of the SWV when it forms; and (ii) calculation results based on it are insensitive to relatively small changes ($\pm0.5°$) to each boundary. As documented by Fu et al. (2015b), the central level of an SWV is around $700\,hPa$, so this level is used to analyze the process of SWV formation in this study. As Figs. 5a–c show, before $t = 24\,h$, no convective systems clearly move out of the TP region. At around $700\,hPa$ (725–$675\,hPa$), the key area of the SWV is dominated by cyclonic vorticity, ascending motion and divergence (Fig. 10a), all of which are weak. By $t = 24$ to $33\,h$, the eastern edge of the primary EMT over the TP has already moved out of the TP, appearing mainly north of $30°N$ (Figs. 5c–f). However, this is not the main reason for the increase in cyclonic vorticity/circulation within the key area of the SWV (Fig. 10a). Instead, the cyclonic vorticity

---

[4] In this study, similarly to Fu et al. (2017), the period from there being no vortex to the point of vortex formation is defined as the formation process of the vortex.
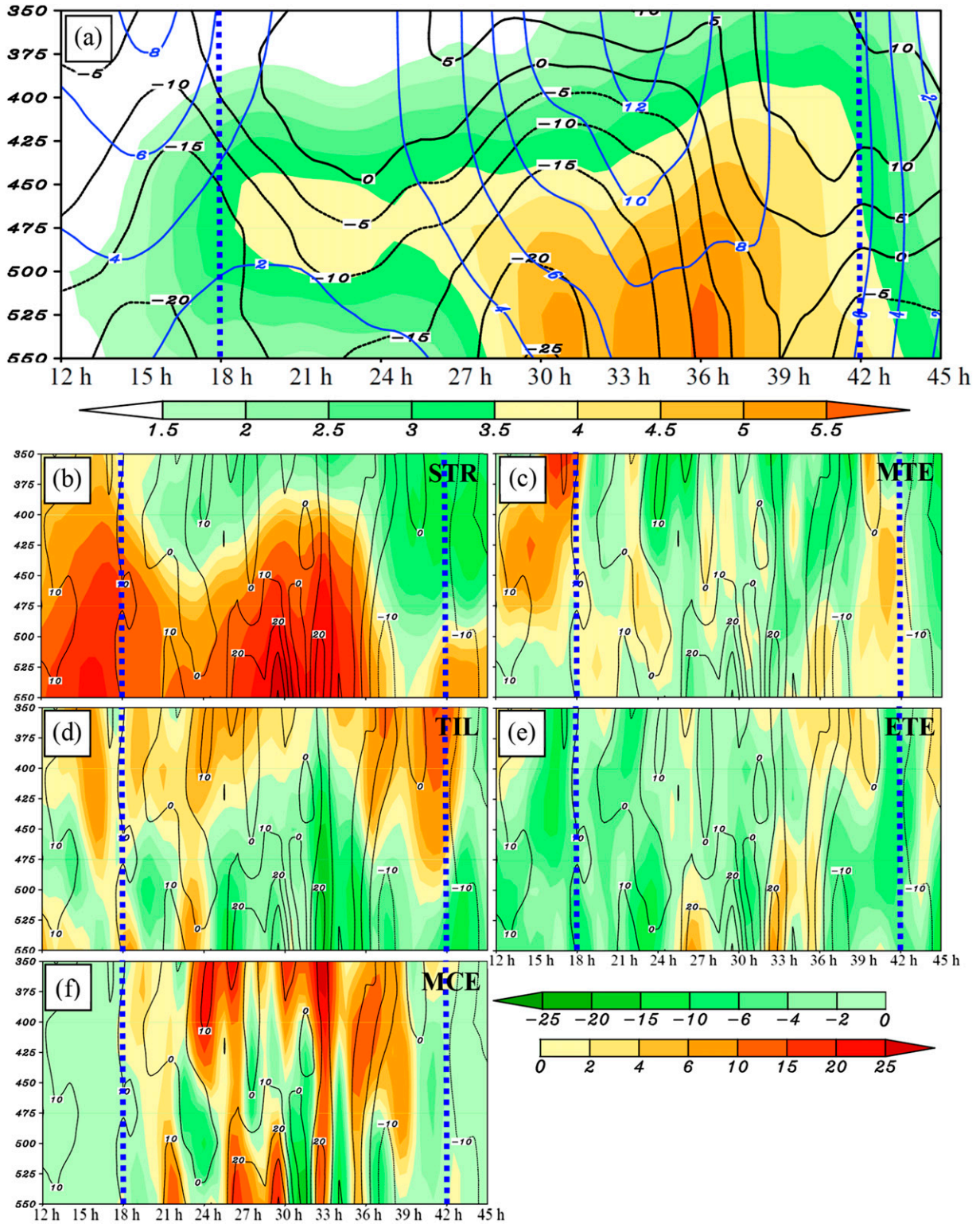
FIG. 9. (a) PLV average vorticity (shading; $10^{-5}\,\mathrm{s}^{-1}$), divergence (black lines; $10^{-6}\,\mathrm{s}^{-1}$), and vertical motions (blue lines; $\mathrm{cm\,s}^{-1}$). (b)–(f) PLV average STR, MTE, TIL, ETE, and MCE, respectively (shading; $10^{-10}\,\mathrm{s}^{-2}$), where the black lines show the total effect of STR + MTE + TIL + ETE + MCE ($10^{-10}\,\mathrm{s}^{-2}$), and the blue dashed lines show the life span of the PLV. The x and y axes are time and pressure (hPa), respectively. Periods before $t = 18\,\mathrm{h}$ are calculated using the key region at $t = 18\,\mathrm{h}$, and periods after $t = 42\,\mathrm{h}$ are calculated using the key region at $t = 42\,\mathrm{h}$.
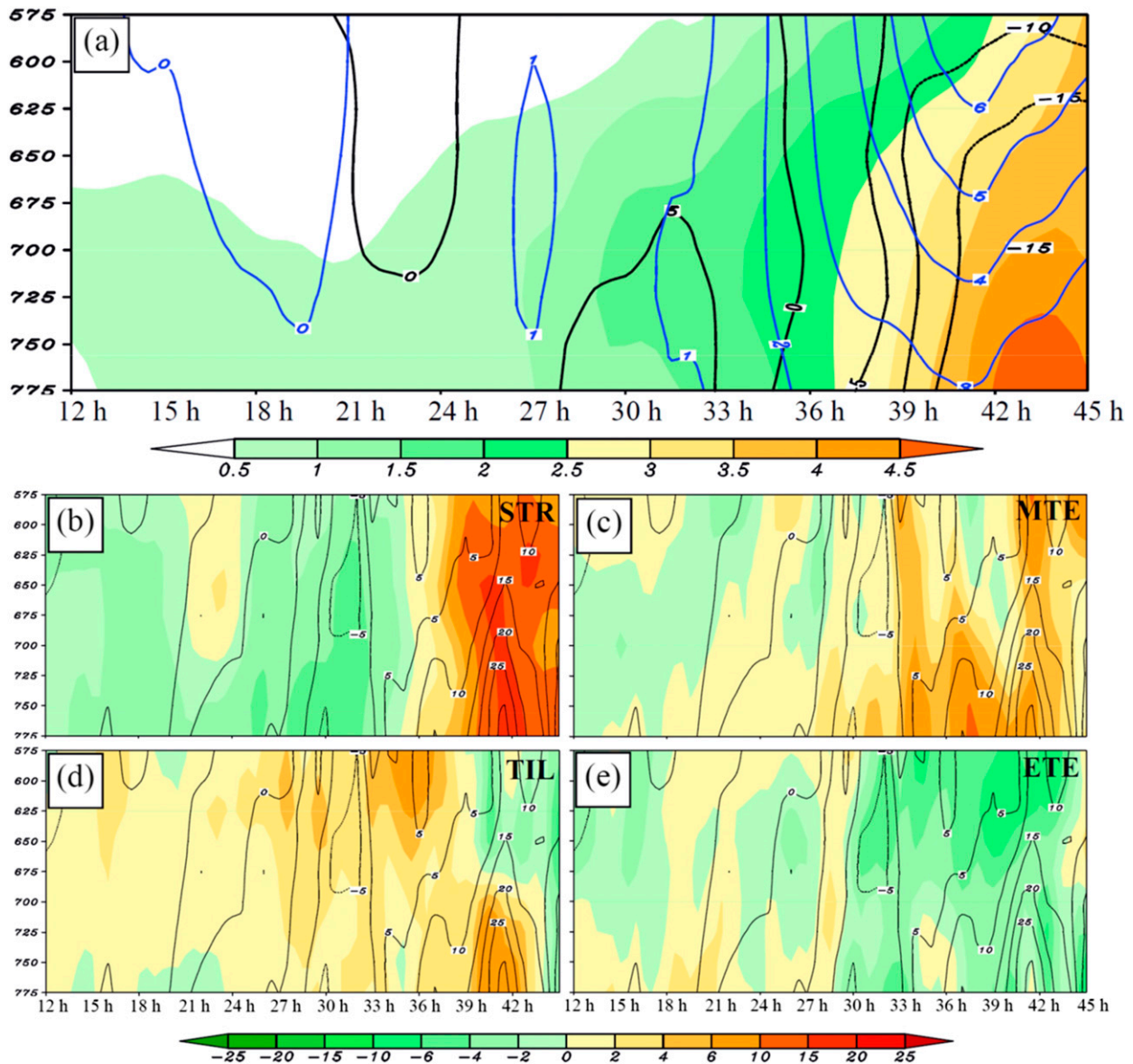
FIG. 10. (a) SWV average vorticity (shading; $10^{-5}\,\mathrm{s}^{-1}$), divergence (black lines; $10^{-6}\,\mathrm{s}^{-1}$), and vertical motions (blue lines; $\mathrm{cm}\,\mathrm{s}^{-1}$). (b)–(e) SWV average STR, MTE, TIL, and ETE, respectively (shading; $10^{-10}\,\mathrm{s}^{-2}$), where the black lines show the total effect of STR + MTE + TIL + ETE ($10^{-10}\,\mathrm{s}^{-2}$). The x and y axes are time and pressure (hPa), respectively.

intensification during this period mainly appears in the southern section (south of 30°N) of the key area (Figs. 8c–f). At $t = 33$ h, the strong vacating stage begins and, from this time to 45 h, the SWV is mainly located ahead of the 500-hPa shortwave trough over the TP (Figs. 5f–j), where warm advection appears (not shown). This promotes ascending motion through quasigeostrophic forcing (Holton 2004) and favors a decrease in pressure (which enhances convergence) at lower levels (Markowski and Richardson 2010); both of these contribute to SWV formation. As the shortwave trough and

the primary EMT vacate the TP, the cyclonic vorticity, ascending motion, and convergence around 700 hPa, within the key area of the SWV, all increase rapidly (Fig. 10a), particularly in regions north of 30°N (Figs. 8f–j).

The budget shows that the cyclonic circulation/vorticity around 700 hPa (725–675 hPa) within the key area of the SWV changes slowly before the strong vacating stage begins (Fig. 10a), since the budget terms are small (gray lines in Fig. 10b). During the strong vacating stage (from $t = 33$ to 45 h), the transport of cyclonic

vorticity by mean flow (i.e., MTE) imports cyclonic vorticity into the SWV key area (Fig. 10c), mainly through northward transport across the southern boundary (Figs. 8g–j); STR intensifies (Fig. 10b), mainly due to increasing convergence in the lower troposphere of the key area (Fig. 10a), particularly in its northern section (north of 30°N); and the tilting (i.e., TIL, Fig. 10d) becomes more intense as the convention strengthens (Fig. 10a). All these factors contribute to SWV formation. In contrast, the transport by the eddy flow (i.e., ETE) mainly causes a net export of cyclonic vorticity from the key area, which is detrimental to SWV formation (Fig. 10e).

Using the latitude of 30°N, the key area of the SWV can be separated into northern and southern sections. Before the strong vacating stage begins, the cyclonic vorticity mainly increases in the southern section of the key area (Figs. 8a–e), where convergence and its associated cyclonic vorticity production increases as a low-level jet appears (Fig. 8e); then, during the strong vacating stage, the northern section shows a more rapid increase (Figs. 8f–j). Vorticity budget (Kirk 2003) calculations indicate that the former is mainly due to northward transport of cyclonic vorticity through the southern boundary of the key area, convergence-induced stretching, and tilting (not shown), all of which are related to the low-level jet (convergence and ascending motion occurs around the northern terminus of the low-level jet). The latter, meanwhile, is mainly caused by horizontal convergence (Fig. 10b), which is affected by the vacating of the primary EMT from the TP (section 5c).

From Figs. 7e–h, it can be seen that: (i) the cyclonic vorticity and positive PV centers associated with the PLV do not vacate the TP and (ii) the cyclonic vorticity and positive PV centers associated with the SWV are newly generated. A meridional-mean cross section (the same as in Fig. 7) through the latitudes of the SWV (28°–33.5°N) also confirms these results (not shown). However, it should be noted that, although the positive PV center associated with the PLV does not vacate the TP, it still affects SWV formation and downstream precipitation. This is discussed in the next section.

5. Impacts of the EMT

a. Effects on downstream precipitation

Precipitation in different simulations (Table 3) is shown Figs. 11a, 12a, 13a, and 14a. Comparing these simulations, it is found that the precipitation in downstream regions east of the TP changes very obviously in the NOSW and NOLH runs. With the downward shortwave flux at the TP surface set to zero in the NOSW

run, the sensible heating is switched off (while the sensible cooling is retained). As a result, the heavy precipitation in downstream regions weakens significantly (e.g., in the Sichuan basin and Hubei Province), and the main rainband at around 31°N moves southward (cf. Figs. 11a and 12a). With the latent heating over the TP removed, the NOLH-simulated precipitation shows similar changes to those in the NOSW run (cf. Figs. 12a and 13a), albeit with larger precipitation amounts. Among the three sensitivity runs (Table 3), the latent heating over the Sichuan basin shows the least influence in downstream regions (partly because the modification in this run is also the smallest), instead mainly reducing the precipitation within and east of the basin (cf. Figs. 11a and 14a).

Overall, as discussed above, apart from local convective activities in downstream regions east of the TP, convective activities over the TP have the most important effect on downstream precipitation. As previous studies (Ye and Gao 1979; Gao et al. 1981; Yanai et al. 1992; Hu and Duan 2015) have shown, there are two important factors influencing convective activity over the TP: (i) condensation-related latent heating and (ii) sensible heating that is related to downward shortwave flux. These two factors are discussed in the following.

When removing latent heating over the TP, no intense convective activity appears there (Figs. 13b,d,e). Ascending motion over the TP is weak, with the composite reflectivity below 35 dBZ. When setting the downward shortwave flux at the surface of the TP to zero, the sensible heating is shut down. This results in a sharp reduction in the intensity and range of convective activity over the TP (Figs. 12b,d,e). However, the primary EMT can still occur, but is much weaker than that in CTRL (cf. Figs. 11d and 12d) and is mainly located around the shortwave trough (Fig. 12b). Corresponding to weaker convective activity, in both the NOLH and NOSW runs, a decrease in temperature, increase in geopotential height, and acceleration of anticyclonic wind perturbation appear over the TP and its surrounding regions (not shown). The changes are more obvious in the NOLH run, because the condensation-related heating is usually larger than the sensible heating. As mentioned above, when the EMT is over the TP, it has a remarkably strong effect on the atmospheric circulation (including the temperature, geopotential height, and wind fields).

b. Effects on the PLV

In the NOLH and NOSW runs, the CTRL-simulated PLV does not form (not shown). This means that strong latent heating associated with intense convective activity is vital for PLV formation (merely weak latent heating such as in NOSW run is not sufficient).
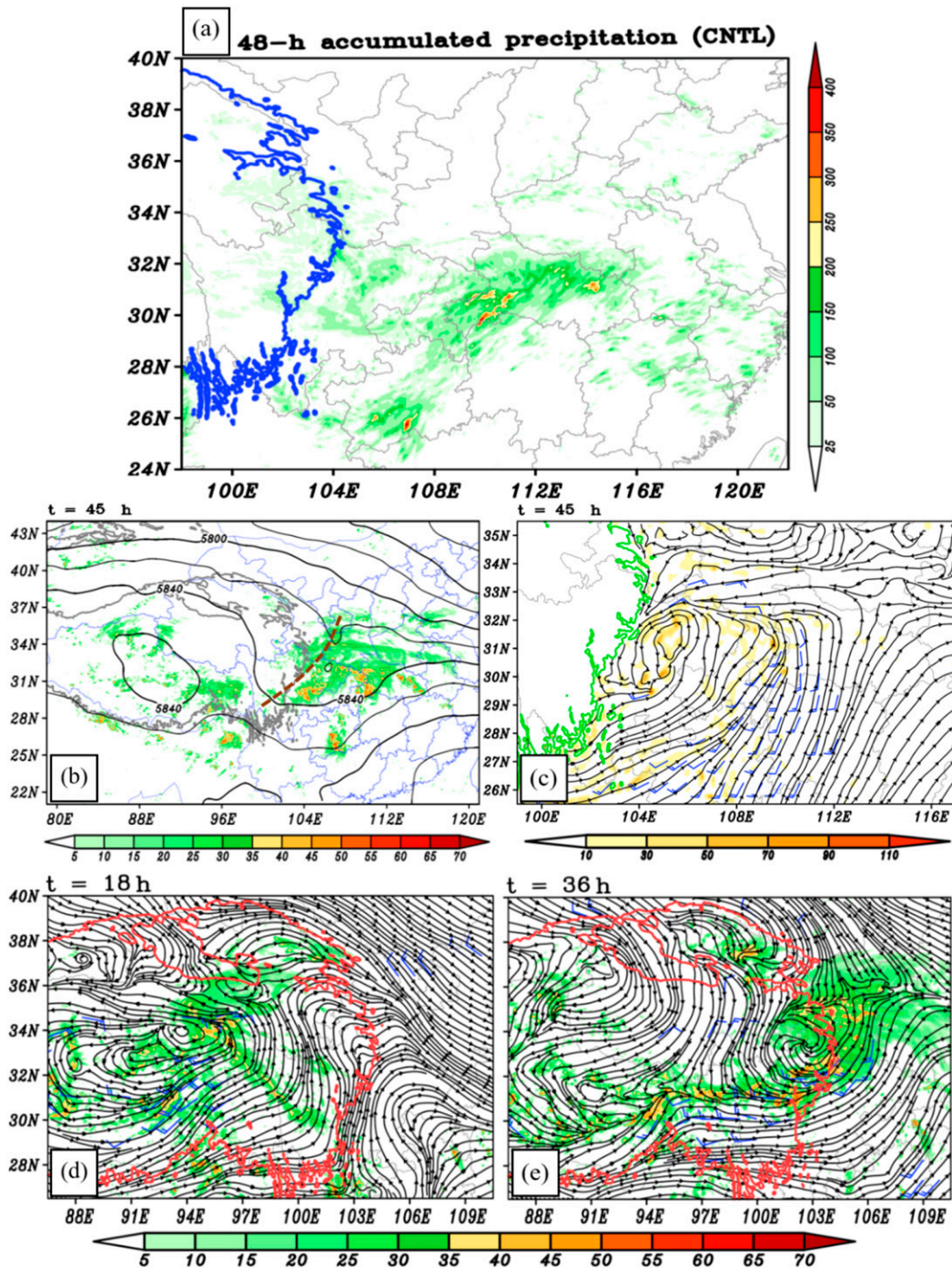
FIG. 11. (a) The 48-h accumulated precipitation (shading; mm), where the blue solid line outlines the TP. (b) Composite reflectivity (shading; dBZ) and 500-hPa geopotential height (black solid line; gpm) at the formation time of the SWV, where the brown dashed line is the trough line and the thick gray line outlines the TP. (c) The 700-hPa stream field, vorticity (shading; $10^{-5}\,s^{-1}$), and wind above $12\,m\,s^{-1}$ (a full barb is $10\,m\,s^{-1}$) at the formation time of the SWV, where the thick green solid line outlines the TP. (d),(e) Composite reflectivity (shading; dBZ), streamline field and wind above $12\,m\,s^{-1}$ at 500-hPa (blue wind barb; a full barb is $10\,m\,s^{-1}$) at the times of the formation and maximum intensity of the PLV, where the thick red solid line outlines the TP. All results are from the CNTL run.
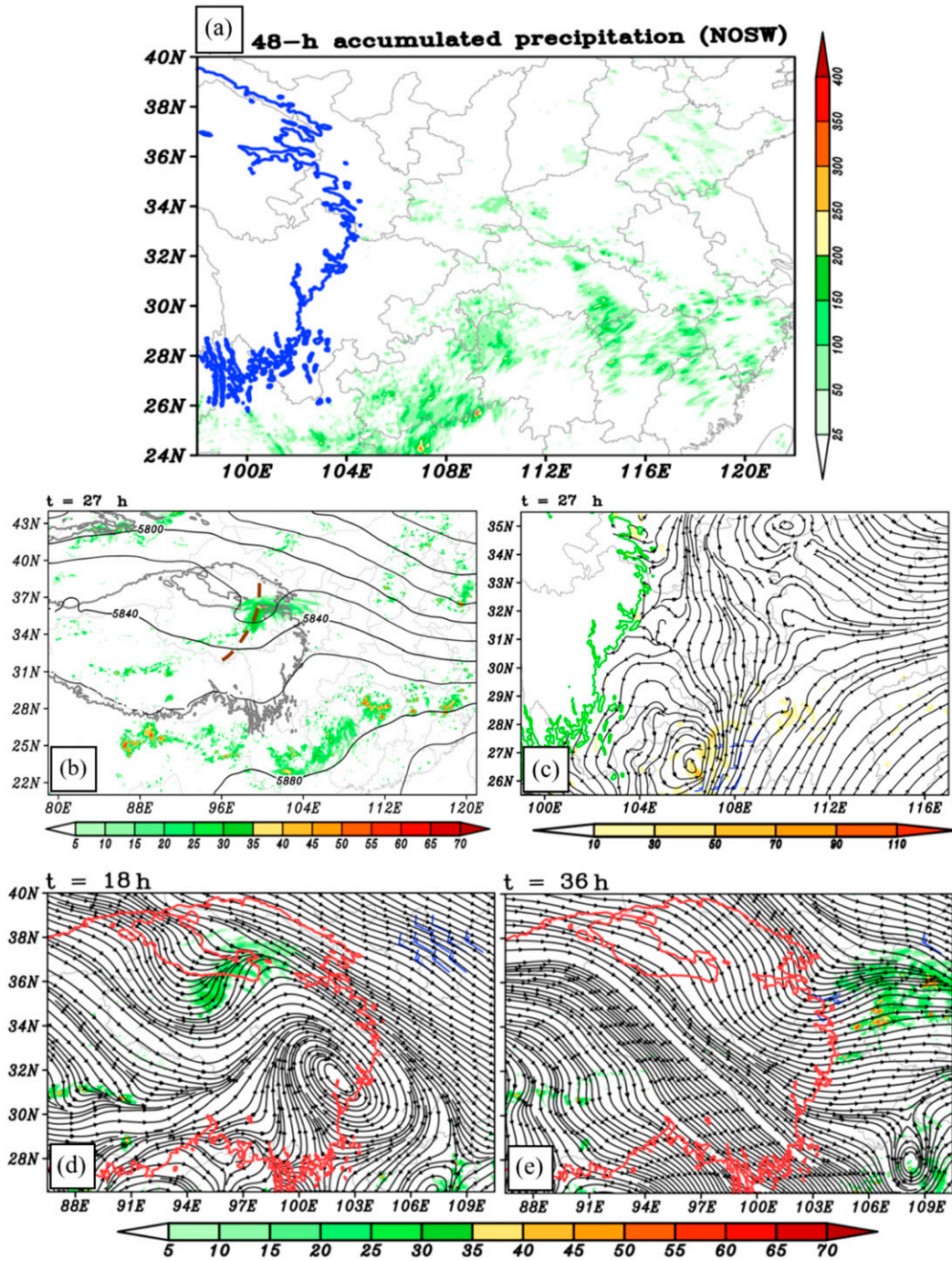
FIG. 12. As in Fig. 11, but for the NOSW run.

According to the positive feedback among convergence, ascending motion and latent heating (Raymond and Jiang 1990), ascending motion and its associated convergence weaken as latent heating weakens. Therefore, the convergence-induced stretching—the dominant factor for the formation/persistence of the CTRL simulated PLV (section 4a)—reduces remarkably.

This explains why the NOLH and NOSW runs do not produce a PLV like that in CTRL.

Comparisons between the NOSW and CTRL runs indicate that sensible heating over the TP enhances ascending motion associated with the EMT to a remarkable extent (cf. Figs. 11d,e and 12d,e). As the PLV in CTRL moves out of the TP region, the sensible heating from the
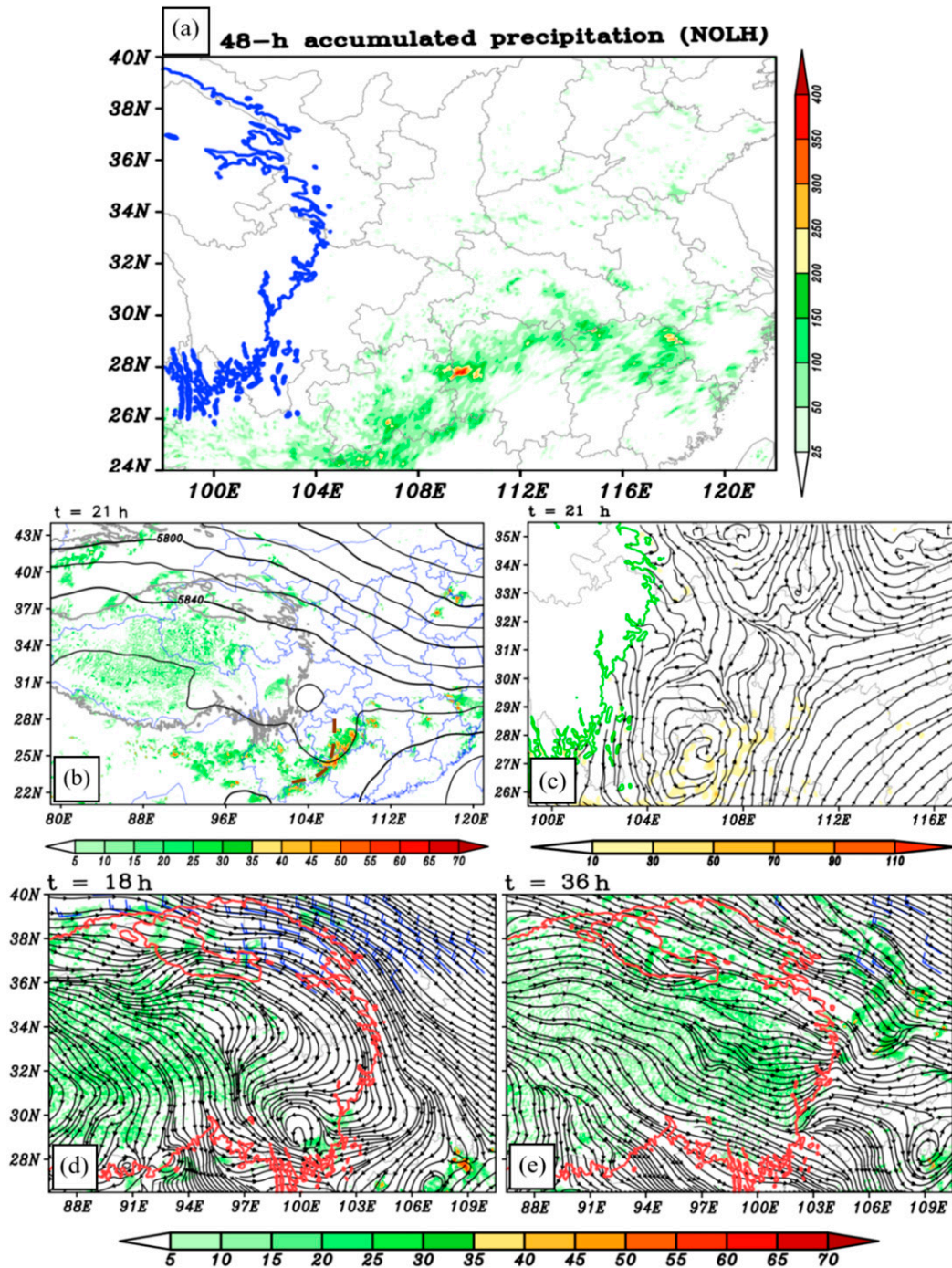
FIG. 13. As in Fig. 11, but for the NOLH run.

TP at the bottom of the vortex reduces rapidly, which in turn induces a rapid weakening of the ascending motion and associated convergence around the PLV (Fig. 9a). This results in a significant decline in the convergence-related STR term, which ultimately results in the dissipation of the PLV.

In contrast to the convective activity over the TP, that over the Sichuan basin shows a much smaller influence on the evolution of the PLV (Figs. 14d,e). As the PLV moves out, its structure changes in the SBOF run, mainly due to the differences in convective activity in the vortex's eastern section. However, the PLVs of the CTRL and SBOF runs both dissipate at $t = 45$ h, through similar mechanisms (not shown), when their main body has vacated the TP region.
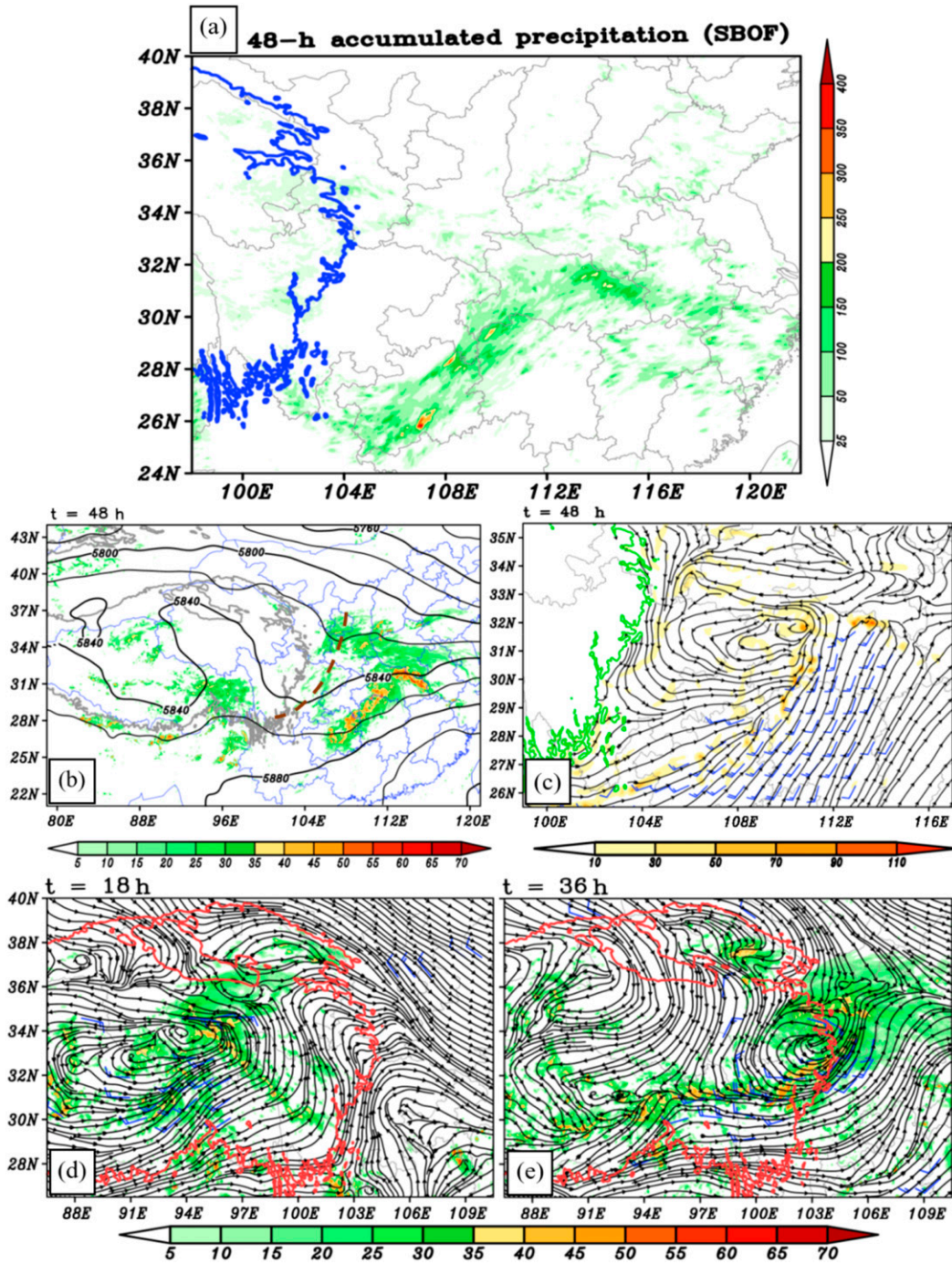
FIG. 14. As in Fig. 11, but for the SBOF run.

c. Effects on the SWV

1) ANALYSIS USING SENSITIVITY RUNS

All three sensitivity runs (Table 3) produce an SWV east of the TP (Figs. 12c, 13c, and 14c). This means that neither the convective activity over the TP nor that over the Sichuan basin is necessary for generating an SWV. Compared to the CTRL-simulated SWV, the NOSW- and NOLH-simulated SWVs form much earlier and at a lower latitude (cf. Figs. 11c, 12c, and 13c). As convective activity over the TP is weakened in the NOSW and NOLH runs, a northeasterly wind perturbation appears southeast of the TP (not shown). It is added to the

southwesterly wind (as in CNTL) at the same location (Figs. 8b,c), generating enhanced convergence in that area. This is also why the main rainbands in the NOLH and NOSW runs are situated at a lower latitude than in CTRL (cf. Figs. 11a, 12a, and 13a).

The SBOF run produces an SWV at a similar time and latitude to that in CTRL (cf. Figs. 11c and 14c). These two SWVs form through similar mechanisms, as described in section 4b. Setting latent heating in the Sichuan basin to zero causes an eastward excursion of the cyclonic vorticity center. The SWVs of the CTRL and SBOF runs mainly move eastward (not shown). Therefore, latent heating in the Sichuan basin does not obviously change the moving direction of the SWV. However, a comparison between Figs. 11c and 14c show that latent heating in the Sichuan basin can enhance the intensity of an SWV. The NOLH- and NOSW-simulated SWVs mainly move northeastward (not shown). This means that convective activity over the TP can change the moving direction of an SWV through its modulation of circulation systems around the TP (section 5b).

The CTRL- and SBOF-simulated SWVs are affected by the primary EMT, and both SWVs form ahead of the shortwave trough that moves out from the TP region (Figs. 11b and 14b). In contrast, the SWVs of the NOSW and NOLH runs show a less clear response to the primary EMT, being mainly affected by a small trough at around 25°N (Figs. 12b and 13b). Overall, the SWVs in all four runs (Table 3) have a common feature: the latitude of the formation location is around the latitude of the shortwave trough (see Figs. 11b,c, 12b,c, 13b,c, and 14b,c).

2) ANALYSIS USING PIECEWISE PV INVERSION

This study utilizes piecewise PV inversion to estimate the direct effects of the EMT on SWV formation (section 2d). As Fig. 15 shows, in the CNTL run, before the strong vacating stage begins, the EMT has produced several positive PV anomaly centers over the TP. The strongest of these is located at around 94°E (at $t = 18$ h), and is closely related to the PLV (cf. Figs. 11d and 15a). As the EMT and PLV move eastward, this positive PV anomaly center also moves eastward and, at $t = 36$ h, both the PLV and PV anomaly center reach their maximum intensity (Figs. 11e and 15e). From $t = 36$ h onward, the positive anomaly center weakens rapidly along with the PLV dissipation.

As demonstrated by the results from the piecewise PV inversion (Figs. 15 and 16), a positive PV anomaly is associated with a cyclonic wind perturbation and negative geopotential height perturbation center (Holton 2004). The former can enhance a cyclonic circulation system directly through superposition, and the latter can have a similar effect because the centripetal pressure

gradient force pointing to the center of the negative height perturbation can enhance convergence and the associated cyclonic vorticity production (through STR). The negative height perturbations associated with the positive PV anomaly centers over the TP cover a larger area than that of the PV anomaly centers themselves (Figs. 15 and 16). In contrast, the positive cyclonic vorticity centers cover a similar area to that of the associated positive anomaly centers. Even if the EMT does not vacate the TP region, it still reduces the geopotential height of downstream regions (Figs. 11d, 15a, and 16a). From $t = 18$ to 36 h, as the EMT moves eastward, the influence of the positive PV anomaly center moves eastward and increases (Figs. 15a–d and 16a–d). Then, from $t = 36$ to 42 h, the height-lowering effect and cyclonic wind perturbation keep moving eastward, but with less intensity following the weakening of the EMT (Figs. 15e–h and 16e–h). By $t = 45$ h, a new PV anomaly center appears at around 500 hPa within the SWV key area (31°N, 106°E, Figs. 15h and 16h). This is associated with a center of geopotential height lowering and cyclonic wind perturbation around 700 hPa, corresponding to the SWV formation (Fig. 11c).

Overall, before the strong vacating stage begins, the strong influences associated with the EMT mainly affect regions outside the key area of the SWV (Figs. 16a–c). This means they are not a dominant factor for the increase in cyclonic vorticity/circulation within the key area. Then, from $t = 33$ h onward, as the EMT changes to moving southeastward, its strong influences extend southward and cover the key area of the SWV (Figs. 16d–h). This contributes to a rapid increase in cyclonic vorticity/circulation within the key area, particularly north of 30°N (Figs. 8g–j). By $t = 42$ h, the central latitude of the maximum influences associated with the EMT is approximately 31°N (Fig. 16g). Three hours later, the SWV forms at around this latitude (Fig. 11c).

To quantitatively evaluate the direct effects associated with the EMT on SWV formation, an average within the key area of the SWV (red box in Fig. 8) is calculated. As Fig. 17 illustrates, the height-lowering effect associated with the EMT starts to affect the SWV key area much earlier than the cyclonic wind perturbation. The latter exerts almost no effect on the key area before the EMT begins to move out (Fig. 17b). The maximum influences associated with the PV anomaly center tends to appear around similar levels to the anomaly center itself. Overall, the height lowering and cyclonic vorticity perturbation both maximize at around 500 hPa and decrease downward (Fig. 17). At around 700 hPa, in the SWV key area, the maximum ratio of the height lowering associated with the EMT to the total height
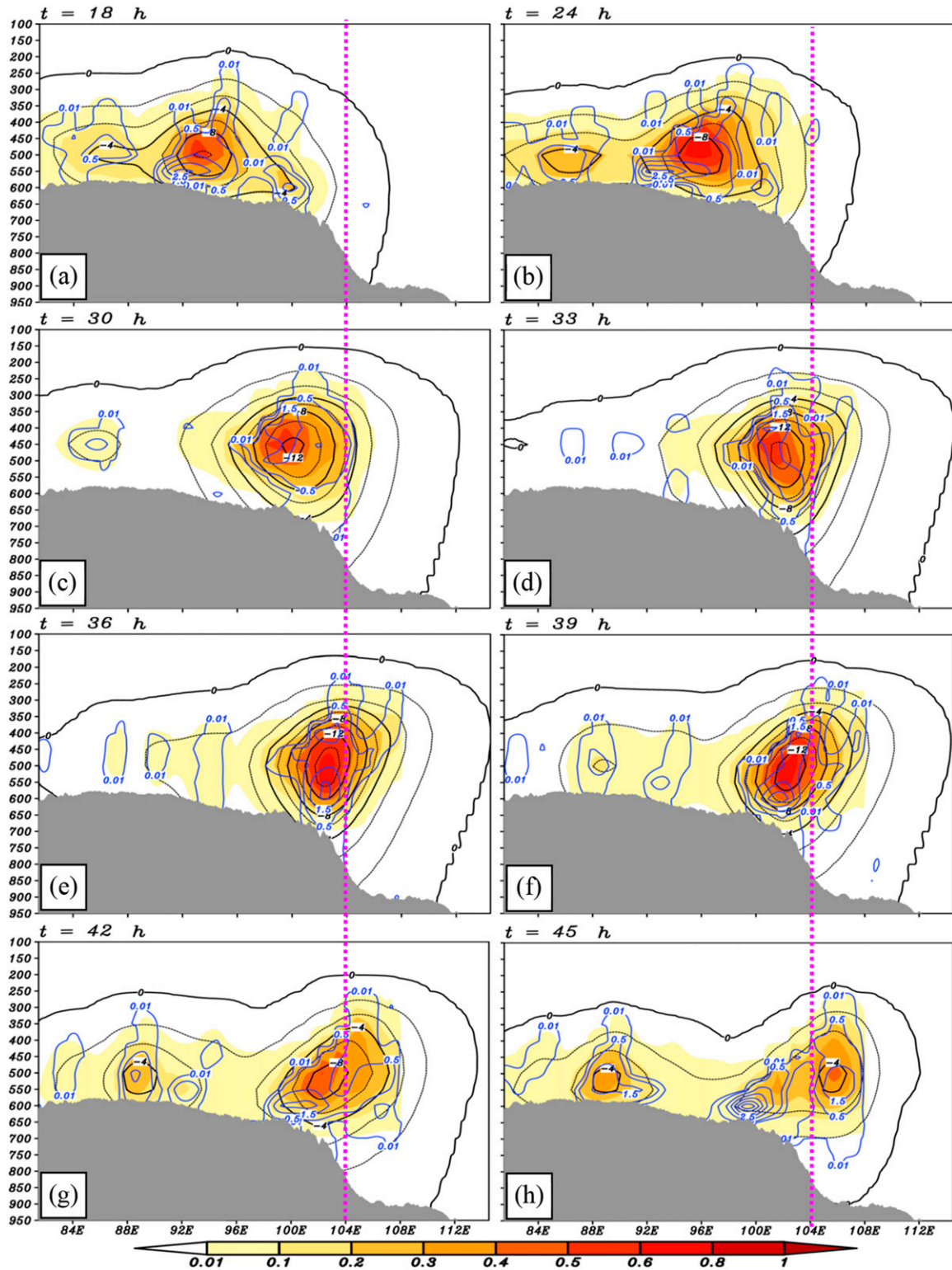
FIG. 15. The CNTL-run meridionally averaged (30°–37°N) PV anomaly (relative to the 60-h mean PV field; shading; PVU), and the associated perturbation height (black lines; gpm; contours are plotted at −18, −16, −14, −12, −10, −8, −6, −4, −2, −0.5, and 0 gpm), and perturbation vorticity (blue solid; $10^{-5}\,\mathrm{s}^{-1}$; contours are plotted at 0.05, 0.5, 1.5, 2.5, 3.5, 4.5, 5.5, and $6.5 \times 10^{-5}\,\mathrm{s}^{-1}$), where the gray shading shows the meridionally averaged topography (m), and the purple dashed lines show the eastern boundary of the TP (104°E).
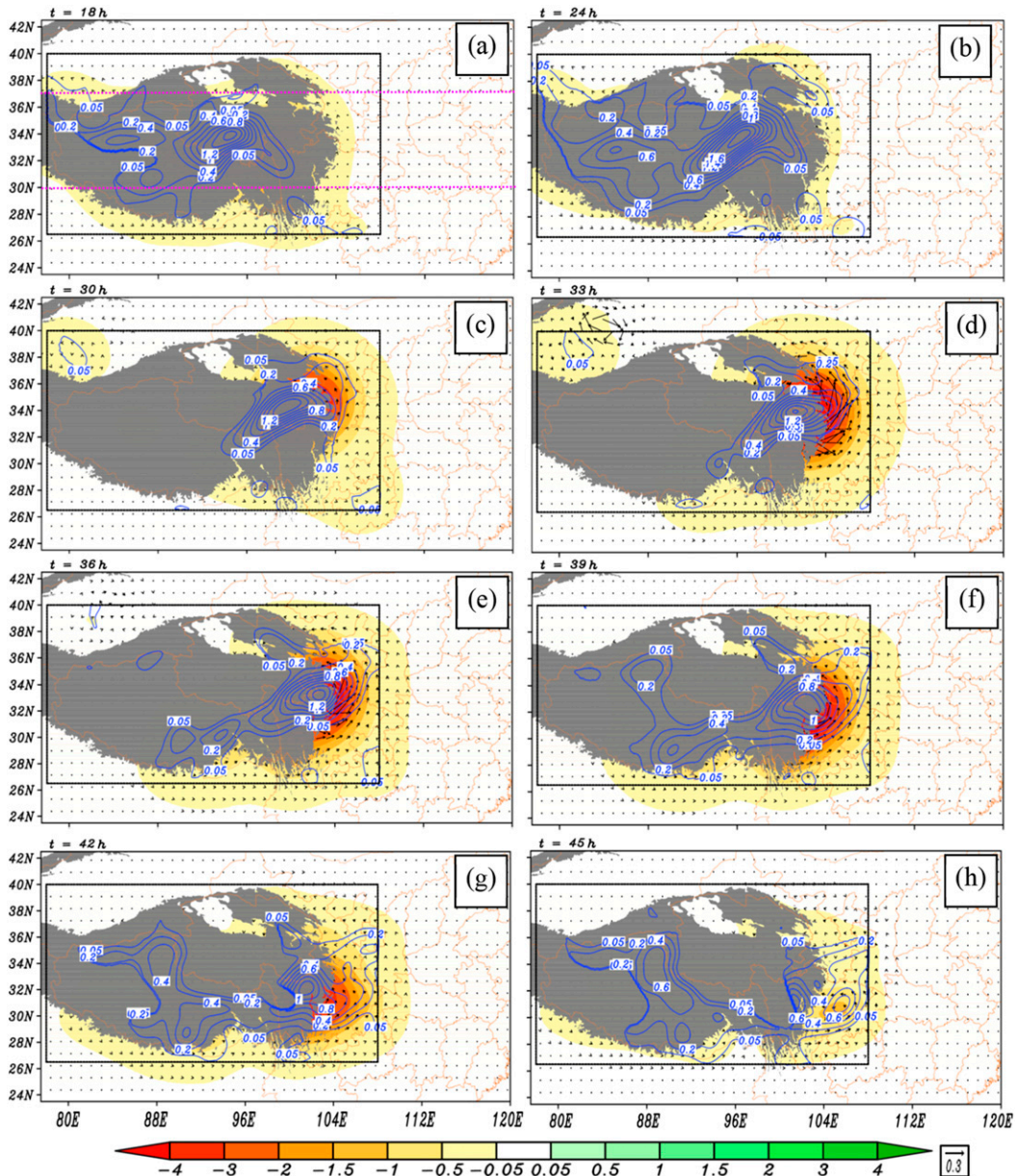
FIG. 16. The CNTL-run simulated 500-hPa PV anomaly (blue solid lines; PVU; contours are plotted at 0.05, 0.2, 0.4, 0.6, 0.8, 1.0, 1.2, 1.4, and 1.6 PVU), the 700-hPa perturbation height (shading; gpm), and the 700-hPa perturbation wind field (vectors; m s^{-1}) associated with the positive PV anomaly due to convective activity over the TP, where the purple dashed lines in (a) show the range used for calculating the meridional mean in Figs. 7 and 15.

anomaly is approximately 10% (Fig. 17a), while its cyclonic vorticity counterpart is around 5% (Fig. 17b). This means that the direct effects associated with the EMT on SWV formation are only of secondary importance.

Aside from direct effects, the EMT might also exert indirect effects on SWV formation. The results of piecewise PV inversion indicate that the EMT is a dominant factor for the evolution of the shortwave trough (not shown). Comparisons between the CTRL

and NOSW runs also confirm this result, as when the EMT weakens substantially (cf. Figs. 11d,e and 12d,e), the intensity of the shortwave trough also reduces sharply (cf. Figs. 5d and 12b). The EMT may therefore affect SWV formation by modulating the shortwave trough that moves out of the TP region [this trough provides favorable conditions for SWV formation through quasigeostrophic forcing (Holton 2004; Fu et al. 2015b)]. Moreover, the EMT might affect SWV formation by
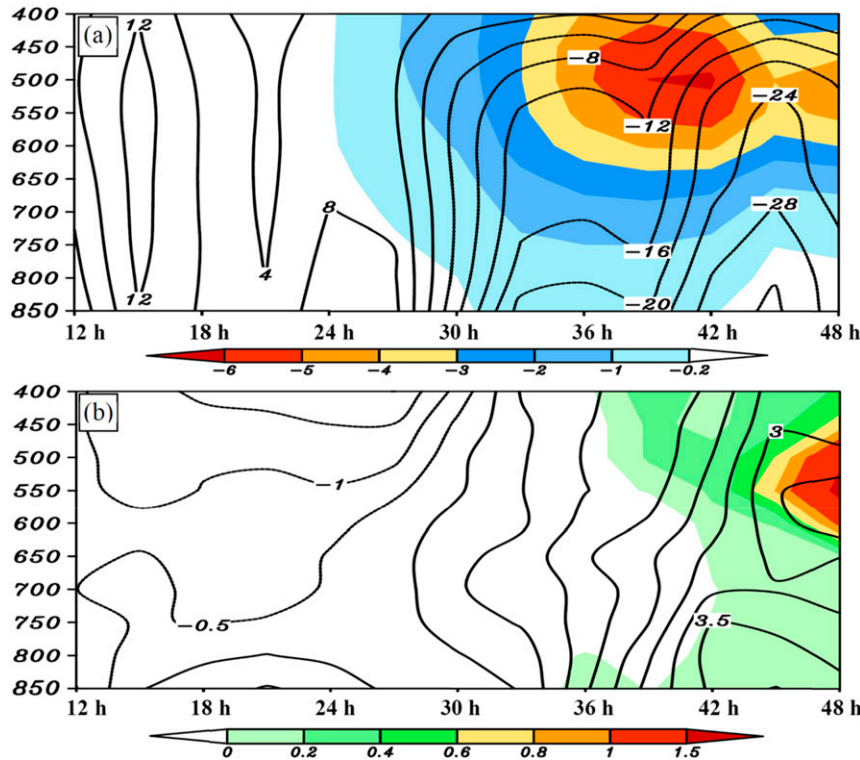
FIG. 17. (a) Time variation of the SWV (28°–33.5°N, 103°–108.5°E) average geopotential height anomaly (relative to the 60-h time mean; black line with an interval of 4 gpm) and the SWV average height perturbation associated with the positive PV anomaly due to convective activities over the TP (shading; gpm). (b) Time variation of the SWV average vorticity anomaly (relative to the 60-h time mean; black line with an interval of $0.5 \times 10^{-5}\,\mathrm{s}^{-1}$) and the SWV average vorticity perturbation associated with the positive PV anomaly due to convective activity over the TP (shading; gpm). All results are from the CNTL run.

enhancing the lower-level convergence within the key area through the height-lowering effect (Figs. 16d–h), since enhancing the lower-level convergence contributes to cyclonic vorticity production and the positive feedback among convergence, ascending motion, and latent heating (Raymond and Jiang 1990).

6. Conclusions and discussion

In this study, the impacts of the EMTs that originate from the TP on PLVs, SWVs, and downstream precipitation are investigated using a series of convection-permitting semi-idealized simulations based on a composite of eight similar events. After confirming the CTRL run has reproduced the salient characteristics of these eight events, a detailed analysis and diagnosis are carried out, with the main findings described in the following.

An EMT can exert important effects on circulation and the associated precipitation in downstream regions through indirect (modulation of the atmospheric circulation including the temperature, geopotential height, and

wind fields, which are shown using sensitivity runs), and direct influences (effects associated with the positive PV produced by the EMT, which are shown using piecewise PV inversion results), even while it is still over the TP. A weaker EMT mainly results in lighter precipitation in downstream regions, with the main rainband located at a lower latitude. This result is consistent with Wang et al. (2014) and Hu and Duan (2015), who focus on the effects of convective activities over the TP on seasonal and interannual temporal scales. At the synoptic scale, Huang et al. (2010) and Sun and Zhang (2012) find convective activity over the TP can affect downstream precipitation through a solenoidal circulation between the TP and its leeside lowlands. In this study, we find that the intensity of the EMT can modify the formation time and initiation location of SWVs, as well as their displacement, which also significantly influences precipitation east of the TP.

Over the TP, the primary EMT is mainly associated with an eastward-moving PLV (from $t = 18$ to 42 h). In our experiments, the CTRL-simulated PLV forms and persists mainly via convergence-induced stretching,

which is closely related to convective activity (ascending motion) via a positive feedback mechanism (Raymond and Jiang 1990). Sensitivity runs show that sensible heating and strong convection-related latent heating are necessary conditions for PLV generation. In contrast, with weak or no latent heating the CTRL-simulated PLV cannot be produced, because the convergence-related cyclonic vorticity production is much weaker. As a PLV vacates the TP, the strong sensible heating from the TP at the bottom of the vortex decreases rapidly with time. This induces a rapid weakening of the ascending motion and its associated convergence around the PLV, which reduces the convergence-related STR term and ultimately results in PLV dissipation and a notable weakening of the primary EMT. This explains why PLVs tend to dissipate over the eastern flank of the TP. After moving out of the TP region (from $t = 45$ h onward), the primary EMT is mainly associated with the lower-level shear line and the SWV. East of the TP, strong convective activity is primarily newly formed, rather than having moved directly out of the TP region.

The formation of the CTRL-simulated SWV experiences two stages: (i) before the strong vacating stage, enhanced cyclonic vorticity mainly occurs in the southern section of the SWV key area, through northward transport, stretching, and tilting, all of which are affected by a low-level jet; and (ii) during the strong vacating stage, rapid enhancement in cyclonic vorticity mainly appears in the northern section of the key area, via convergence-induced stretching, which is influenced by the primary EMT.

Piecewise PV inversion shows that the EMT contributes to SWV formation directly by causing a cyclonic wind perturbation and height lowering around the Sichuan basin (these two effects are associated with the positive PV anomaly that is produced by the EMT-related latent heating). These two impacts initiate as the EMT is still over the TP. During the strong vacating stage, as the positive PV anomaly center has already moved to the eastern flank of the TP, these two impacts enhance substantially within the key area of the SWV. However, neither of them is a dominant factor for SWV formation. This result is consistent with the results derived from the sensitivity runs (i.e., convective activity over the TP is not a necessary condition for SWV formation). This result is also consistent with those documented in Wang and Tan (2014), who find that tilting of southwesterly airflow by the Hengduan Cordillera (rather than the EMT) plays a dominant role in SWV formation. Aside from direct influences, the EMT might also affect SWV formation indirectly, by modulating the shortwave trough that moves out from the TP region, and by enhancing the lower-level convergence.

APPENDIX A

Standards for Defining a Mesoscale Convective System (MCS)

a. Observed MCSs

Satellite blackbody temperature T_{BB} data from *Himawari-8* (Bessho et al. 2016) are used for tracking the moving-eastward-and-vacating-the-TP type of MCSs (i.e., EMTs). This study detects the MCSs by using the region-growing method (Li 2010; Wang et al. 2010). An MCS generated over the TP is defined as follows:

1) it must form within the region 26°–40°N, 75°–103°E, with an altitude exceeding 3000 m; this guarantees that it is generated over the TP;
2) its cloud area with $T_{BB} \leq -52$°C must exceed 5000 km^2 (Mathon and Laurent 2001; Zheng et al. 2008);
3) condition 2 must be satisfied for at least three consecutive hours (Parker and Johnson 2000).

The time at which a confirmed MCS meets condition 2 for the first time is defined as its formation time, and the time at which an MCS either no longer meets condition 2 or merges with a larger MCS is defined as its dissipation time. The location of the centroid of an MCS is taken as its location.

b. Simulated MCSs

The simulated composite reflectivity is used for tracking the simulated MCSs. The MCSs are detected by using the region-growing method (Li 2010; Wang et al. 2010). An MCS that is generated over the TP is defined as follows:

1) it must form within the region 26°–40°N, 75°–103°E, with an altitude exceeding 3000 m; this guarantees that it is generated over the TP;

2) its 30-dBZ contiguous echo coverage must exceed a 30 km × 30 km area with a maximum exceeding 45 dBZ for at least 1 h (Zheng et al. 2013).

The time at which a confirmed MCS satisfies the intensity and area criteria in condition 2 for the first time is defined as its formation time, and the time at which it either no longer meets the intensity and area criteria in condition 2 or merges with a larger MCS is defined as its dissipation time. The location of the centroid of an MCS is taken as its location.

APPENDIX B

Methods for Tracking EMTs

a. Automatic tracking algorithm

We use the automatic tracking algorithm developed by Li (2010) to track the observed and simulated MCSs, which involves five main procedures:

1) read T_{BB}/reflectivity data at time t, and use the nine-point smoothing method to remove noise interference;

2) identify MCSs (based on the T_{BB}/reflectivity data, using the region-growing method) according to the MCS intensity and area criteria shown in appendix A, and obtain key features of the MCSs at time t;

3) read data at time $t + 1$ and repeat steps 1 and 2;

4) match MCSs detected at times t and $t + 1$ [the following three standards are used to match MCSs: (i) the distance standard—from time t to $t + 1$, the displacement of an MCS center should be less than 165 km h^{-1}; (ii) the R-descriptor standard (Lu et al. 1987), which is approximately invariant during translation, rotation, and scaling of an MCS; and (iii) the Hu-moment standard (Hu 1962), which is effective for shape recognition];

5) loop steps 1–4 until the end of the study period.

b. Manual correction

Based on the correction methods documented in Mathon and Laurent (2001) and Feng et al. (2012), the manual correction method in this study includes three key points:

1) when two or more MCSs merge together, the merged MCS is assumed to be the continuation of the largest MCS, while the smaller MCSs are terminated;

2) when an MCS splits into several smaller parts, the largest part is assumed to continue tracking as the original system and the smaller parts are assumed as the formation of new MCSs if they satisfy the MCS criterion;

3) the corrected MCSs must satisfy the criteria used in the automatic tracking algorithm.

APPENDIX C

Objective Methods to Define and Track PLVs

Based on previous studies (Gao et al. 1981; Shen et al. 1986; Zhao et al. 2004; Feng et al. 2014), a PLV in this study is defined as follows:

1) it must form within the region 26°–40°N, 75°–103°E, with an altitude exceeding 3000 m; this guarantees that it is generated over the TP;

2) it must have a significant vortex structure, including a closed cyclonic stream field structure and a clear associated cyclonic vorticity region (vorticity ≥ 2 × 10^{-5} s^{-1}) (Curio et al. 2019), which is located within the vortex circulation and accounts for at least 1/3 of its area;

3) the diameter of the vortex must be greater than 200 km (the lower limit of a meso-α-scale system) and less than 800 km (Feng et al. 2014);

4) it must last for at least 6 h.

In this study, both the observed and simulated PLVs are detected manually using the above standards. The tracking of a PLV is also conducted manually, based on the following standards:

1) a PLV moving direction must be mainly along the direction of the mean 500-hPa wind within and around the vortex;

2) between two successive time steps (for the CFSR data, we interpolate the 6-hourly data linearly to 3-hourly resolution for tracking, while for the simulation, we use hourly output from WRF for tracking), the moving speed of the center of a vortex cannot exceed 75 km h^{-1} (Fu et al. 2016);

3) when splitting occurs, the larger section is regarded as the original PLV for subsequent tracking;

4) when merging occurs, the PLV will be regarded as dissipated if it merged into a much bigger vortex, whereas if the PLV is much larger than the other vortex, the merged vortex will be regarded as the original PLV for subsequent tracking.

REFERENCES

Bessho, K., and Coauthors, 2016: An introduction to Himawari-8/9—Japan's new-generation geostationary meteorological satellites. *J. Meteor. Soc. Japan*, **94**, 151–183, https://doi.org/10.2151/jmsj.2016-009.

Charney, J. G., 1955: The use of primitive equations of motion in numerical prediction. *Tellus*, **7**, 22–26, https://doi.org/10.3402/tellusa.v7i1.8772.

Chen, F., and J. Dudhia, 2001: Coupling an advanced land surface–hydrology model with the Penn State–NCAR MM5 modeling system. Part I: Model implementation and sensitivity. *Mon. Wea. Rev.*, **129**, 569–585, https://doi.org/10.1175/1520-0493(2001)129<0569:CAALSH>2.0.CO;2.

Chen, L., E. Reiter, and Z. Feng, 1985: The atmospheric heat source over the Tibetan Plateau: May–August 1979. *Mon. Wea. Rev.*, **113**, 1771–1790, https://doi.org/10.1175/1520-0493(1985)113<1771:TAHSOT>2.0.CO;2.

Chen, L. T., and R. Wu, 2000: Interannual and decadal variations of snow cover over Qinghai-Xizang Plateau and their relationships to summer monsoon rainfall in China. *Adv. Atmos. Sci.*, **17**, 18–30, https://doi.org/10.1007/s00376-000-0040-7.

Curio, J., R. Schiemann, K. I. Hodges, and A. G. Turner, 2019: Climatology of Tibetan Plateau vortices in reanalysis data and a high-resolution global climate model. *J. Climate*, **32**, 1933–1950, https://doi.org/10.1175/JCLI-D-18-0021.1.

Davis, C. A., and K. A. Emanuel, 1991: Potential vorticity diagnostics of cyclogenesis. *Mon. Wea. Rev.*, **119**, 1929–1953, https://doi.org/10.1175/1520-0493(1991)119<1929:PVDOC>2.0.CO;2.

——, and T. J. Galarneau, 2009: The vertical structure of mesoscale convective vortices. *J. Atmos. Sci.*, **66**, 686–704, https://doi.org/10.1175/2008JAS2819.1.

Ding, Y., 1993: *Study on the Lasting Heavy Rainfalls over the Yangtze-Huaihe River Basin in 1991.* China Meteorological Press, 255 pp.

Duan, A., and G. Wu, 2005: Role of the Tibetan Plateau thermal forcing in the summer climate patterns over subtropical Asia. *Climate Dyn.*, **24**, 793–807, https://doi.org/10.1007/s00382-004-0488-8.

——, M. Wang, Y. Lei, and Y. Cui, 2013: Trends in summer rainfall over China associated with the Tibetan Plateau sensible heat source during 1980–2008. *J. Climate*, **26**, 261–275, https://doi.org/10.1175/JCLI-D-11-00669.1.

Ertel, H., 1942: Ein neuer hydrodynamischer wirbelsatz (A new hydrodynamic vorticity). *Meteor. Z.*, **59**, 271–281.

Feng, X., C. Liu, R. Rasmussen, and G. Fan, 2014: A 10-yr climatology of Tibetan Plateau vortices with NCEP Climate Forecast System Reanalysis. *J. Appl. Meteor. Climatol.*, **53**, 34–46, https://doi.org/10.1175/JAMC-D-13-014.1.

Feng, Z., X. Dong, B. Xi, S. A. McFarlane, A. Kennedy, B. Lin, and P. Minnis, 2012: Life cycle of midlatitude deep convective systems in a Lagrangian framework. *J. Geophys. Res.*, **117**, D23201, https://doi.org/10.1029/2011JD017012.

Fu, S.-M., and J.-H. Sun, 2012: Circulation and eddy kinetic energy budget analyses on the evolution of a Northeast China Cold Vortex (NCCV) in May 2010. *J. Meteor. Soc. Japan*, **90**, 553–573, https://doi.org/10.2151/jmsj.2012-408.

——, ——, S.-X. Zhao, and W.-L. Li, 2010: The impact of the eastward propagation of convective systems over the Tibetan Plateau on southwest vortex formation in summer. *Atmos. Oceanic Sci. Lett.*, **3**, 51–57, https://doi.org/10.1080/16742834.2010.11446836.

——, ——, ——, ——, and B. Li, 2011: A study of the impacts of the eastward propagation of convective cloud systems over the Tibetan Plateau on the rainfall of the Yangtze-Huai River basin. *Acta Meteor. Sin.*, **69**, 581–600.

——, ——, and J.-R. Sun, 2014: Accelerating two-stage explosive development of an extratropical cyclone over the northwest-

ern Pacific Ocean: A piecewise potential vorticity diagnosis. *Tellus*, **66A**, 23210, https://doi.org/10.3402/tellusa.v66.23210.

——, W.-L. Li, and J. Ling, 2015a: On the evolution of a long-lived mesoscale vortex over the Yangtze River Basin: Geometric features and interactions among systems of different scales. *J. Geophys. Res. Atmos.*, **120**, 11 889–11 917, https://doi.org/10.1002/2015JD023700.

——, ——, J.-H. Sun, J.-P. Zhang, and Y.-C. Zhang, 2015b: Universal evolution mechanisms and energy conversion characteristics of long-lived mesoscale vortices over the Sichuan Basin. *Atmos. Sci. Lett.*, **16**, 127–134, https://doi.org/10.1002/asl2.533.

——, J.-P. Zhang, J.-H. Sun, and T.-B. Zhao, 2016: Composite analysis of long-lived mesoscale vortices over the middle reaches of the Yangtze River valley: Octant features and evolution mechanisms. *J. Climate*, **29**, 761–781, https://doi.org/10.1175/JCLI-D-15-0175.1.

——, J.-H. Sun, Y.-L. Luo, and Y.-C. Zhang, 2017: Formation of long-lived summertime mesoscale vortices over central east China: Semi-idealized simulations based on a 14-year vortex statistic. *J. Atmos. Sci.*, **74**, 3955–3979, https://doi.org/10.1175/JAS-D-16-0328.1.

Fujinami, H., and T. Yasunari, 2001: The seasonal and intraseasonal variability of diurnal cloud activity over the Tibetan Plateau. *J. Meteor. Soc. Japan*, **79**, 1207–1227, https://doi.org/10.2151/jmsj.79.1207.

Gao, Y., M. Tang, S. Luo, Z. Shen, and C. Li, 1981: Some aspects of recent research on the Qinghai-Xizang Plateau meteorology. *Bull. Amer. Meteor. Soc.*, **62**, 31–35, https://doi.org/10.1175/1520-0477(1981)062<0031:SAORRO>2.0.CO;2.

He, G., W. Gao, and N. Tu, 2009: The dynamic diagnosis on eastward moving characteristics and developing mechanism of two Tibetan Plateau vortex processes. *Acta Meteor. Sin.*, **67**, 599–612.

Holton, J. R., 2004: *An Introduction to Dynamic Meteorology.* Academic Press, 552 pp.

Hong, S.-Y., and J.-O. Lim, 2006: The WRF single-moment microphysics scheme (WSM6). *J. Korean Meteor. Soc.*, **42**, 129–151.

Hu, J., and A. M. Duan, 2015: Relative contributions of the Tibetan Plateau thermal forcing and the Indian Ocean Sea surface temperature basin mode to the interannual variability of the East Asian summer monsoon. *Climate Dyn.*, **45**, 2697–2711, https://doi.org/10.1007/s00382-015-2503-7.

Hu, L., D. Deng, S. Gao, and X. Xu, 2016: The seasonal variation of Tibetan convective systems: Satellite observation. *J. Geophys. Res. Atmos.*, **121**, 5512–5525, https://doi.org/10.1002/2015JD024390.

——, ——, X. Xu, and P. Zhao, 2017: The regional differences of Tibetan convective systems in boreal summer. *J. Geophys. Res. Atmos.*, **122**, 7289–7299, https://doi.org/10.1002/2017JD026681.

Hu, M. K., 1962: Visual pattern recognition by moment invariants. *IEEE Trans. Inf. Theory*, **28**, 179–187, https://doi.org/10.1109/TIT.1962.1057692.

Huang, H., C. Wang, G. T. Chen, and R. E. Carbone, 2010: The role of diurnal solenoidal circulation on propagating rainfall episodes near the Eastern Tibetan Plateau. *Mon. Wea. Rev.*, **138**, 2975–2989, https://doi.org/10.1175/2010MWR3225.1.

Jiang, J., and M. Fan, 2002: Convective clouds and mesoscale convective systems over the Tibetan Plateau in summer. *Chin. J. Atmos. Sci.*, **26**, 263–270.

——, X. Xiang, and M. Fan, 1996: The spatial and temporal distributions of severe mesoscale convective systems over

Tibetan Plateau in Summer (in Chinese). *Acta Meteor. Sin.*, **4**, 473–478.

Jiang, X., Y. Li, S. Yang, K. Yang, and J. Chen, 2016: Interannual variation of summer atmospheric heat source over the Tibetan Plateau and the role of convection around the western Maritime Continent. *J. Climate*, **29**, 121–138, https://doi.org/10.1175/JCLI-D-15-0181.1.

Kain, J. S., 2004: The Kain–Fritsch convective parameterization: An update. *J. Appl. Meteor.*, **43**, 170–181, https://doi.org/10.1175/1520-0450(2004)043<0170:TKCPAU>2.0.CO;2.

Kirk, J. R., 2003: Comparing the dynamical development of two mesoscale convective vortices. *Mon. Wea. Rev.*, **131**, 862–890, https://doi.org/10.1175/1520-0493(2003)131<0862:CTDDOT>2.0.CO;2.

Koshyk, J. N., and N. A. McFarlane, 1996: The potential vorticity budget of an atmospheric general circulation model. *J. Atmos. Sci.*, **53**, 550–563, https://doi.org/10.1175/1520-0469(1996)053<0550:TPVBOA>2.0.CO;2.

Li, G.-P., F.-H. Zhao, C.-H. Huang, and J.-L. Niu, 2014: Analysis of 30-year climatology of the Tibetan Plateau vortex in summer with NCEP reanalysis data. *Chin. J. Atmos. Sci.*, **38**, 756–769, https://doi.org/10.3878/j.issn.1006-9895.2013.13235.

——, H.-G. Lu, C.-H. Huang, Y.-Y. Fan, and B. Zhang, 2016: A climatology of the surface heat source on the Tibetan Plateau in summer and its impacts on the formation of the Tibetan Plateau vortex. *Chin. J. Atmos. Sci.*, **40**, 131–141.

Li, J., 2010: Study on the characteristics of the mesoscale convective cloud clusters occurred in east Asia during warm seasons (in Chinese). Ph.D. dissertation, Institute of Atmospheric Physics, Chinese Academy of Sciences, 154 pp.

——, D. Wang, and B. Wang, 2012: Structure characteristics of moist neutral stratification in a mesoscale convective system (in Chinese). *Climate Environ. Res.*, **17**, 617–627.

Li, Y., Y. Wang, Y. Song, L. Hu, S. Gao, and F. Rong, 2008: Characteristics of summer convective systems initiated over the Tibetan Plateau. Part I: Origin, track, development, and precipitation. *J. Appl. Meteor. Climatol.*, **47**, 2679–2695, https://doi.org/10.1175/2008JAMC1695.1.

Lu, L., G. Zhou, and Z. Zhang, 1995: Direct and global solar radiations in the region of Mt. Qomolangma during the summer 1992. *Taiyang Neng Xuebao*, **3**, 229–233.

Lu, X., J. Ma, and C. Wu, 1987: A shape analytical method of two dimensional objects. *J. Chin. Inst. Comm.*, **8**, 61–67.

Markowski, P., and Y. Richardson, 2010: *Mesoscale Meteorology in Midlatitudes*. Wiley-Blackwell, 407 pp.

Mathon, V., and H. Laurent, 2001: Life cycle of Sahelian mesoscale convective cloud systems. *Quart. J. Roy. Meteor. Soc.*, **127**, 377–406, https://doi.org/10.1002/qj.49712757208.

McTaggart-Cowan, R., T. J. Galarneau Jr., L. F. Bosart, and J. A. Milbrandt, 2010: Development and tropical transition of an alpine lee cyclone. Part I: Case analysis and evaluation of numerical guidance. *Mon. Wea. Rev.*, **138**, 2281–2307, https://doi.org/10.1175/2009MWR3147.1.

Ni, C.-C., G.-P. Li, and X.-Z. Xiong, 2017: Analysis of a vortex precipitation event over Southwest China using AIRS and in situ measurements. *Adv. Atmos. Sci.*, **34**, 559–570, https://doi.org/10.1007/s00376-016-5262-4.

Noh, Y., W. G. Cheon, and S. Raasch, 2001: The improvement of the K-profile model for the PBL using LES. Preprints, *Int. Workshop of Next Generation NWP Model*, Seoul, South Korea, Laboratory for Atmospheric Modeling Research, 65–66.

Parker, M. D., and R. H. Johnson, 2000: Organizational modes of midlatitude mesoscale convective systems. *Mon. Wea. Rev.*,

128, 3413–3436, https://doi.org/10.1175/1520-0493(2001)129<3413:OMOMMC>2.0.CO;2.

Qin, D.-Y., Z.-Y. Fang, and J.-X. Jiang, 2006: The cloud systems of heavy rainfall in the typical Meiyu Period and their interactions. *Chin. J. Atmos. Sci.*, **30**, 578–586, https://doi.org/10.3878/j.issn.1006-9895.2006.04.04.

Rangwala, I., J. Miller, and M. Xu, 2009: Warming in the Tibetan Plateau: Possible influences of the changes in surface water vapor. *Geophys. Res. Lett.*, **36**, 295–311, https://doi.org/10.1029/2009GL037245.

Raymond, D., and H. Jiang, 1990: A theory for long-lived mesoscale convective systems. *J. Atmos. Sci.*, **47**, 3067–3077, https://doi.org/10.1175/1520-0469(1990)047<3067:ATFLLM>2.0.CO;2.

Saha, S., and Coauthors, 2014: The NCEP Climate Forecast System version 2. *J. Climate*, **27**, 2185–2208, https://doi.org/10.1175/JCLI-D-12-00823.1.

Schär, C., 1990: Quasi-geostrophic lee cyclogenesis. *J. Atmos. Sci.*, **47**, 3044–3066, https://doi.org/10.1175/1520-0469(1990)047<3044:QGLC>2.0.CO;2.

Shen, R., E. R. Reiter, and J. F. Bresch, 1986: Numerical simulation of the development of vortices over the Qinghai-Xizang (Tibet) Plateau. *Meteor. Atmos. Phys.*, **35**, 70–95, https://doi.org/10.1007/BF01029526.

Skamarock, W. C., and Coauthors, 2008: A description of the Advanced Research WRF version 3. NCAR Tech. Note NCAR/TN-475+STR, 113 pp., https://doi.org/10.5065/D68S4MVH.

Sun, J.-H., and F. Zhang, 2012: Impacts of mountain–plains solenoid on diurnal variations of rainfalls along the mei-yu front over the East China plains. *Mon. Wea. Rev.*, **140**, 379–397, https://doi.org/10.1175/MWR-D-11-00041.1.

Tao, S.-Y., 1980: *Rainstorms in China*. Science Press, 225 pp.

Wang, B., 1987: The development mechanism for Tibetan Plateau warm vortices. *J. Atmos. Sci.*, **44**, 2978–2994, https://doi.org/10.1175/1520-0469(1987)044<2978:TDMFTP>2.0.CO;2.

Wang, C., and G. T. Chen, 2002: Case study of the leeside mesolow and mesocyclone in TAMEX. *Mon. Wea. Rev.*, **130**, 2572–2592, https://doi.org/10.1175/1520-0493(2002)130<2572:CSOTLM>2.0.CO;2.

Wang, G.-L., L.-P. Liu, Z. Ruan, H.-Y. Wang, and Q.-P. Chen, 2010: Storm identification, tracking and nowcasting techniques based on the radar mosaic data. *Plateau Meteor.*, **29**, 1546–1555.

Wang, Q.-W., and Z.-M. Tan, 2014: Multi-scale topographic control of southwest vortex formation in Tibetan Plateau region in an idealized simulation. *J. Geophys. Res. Atmos.*, **119**, 543–11, https://doi.org/10.1002/2014JD021898.

Wang, Z. Q., A. M. Duan, and G. X. Wu, 2014: Time-lagged impact of spring sensible heat over the Tibetan Plateau on the summer rainfall anomaly in East China: Case studies using the WRF model. *Climate Dyn.*, **42**, 2885–2898, https://doi.org/10.1007/s00382-013-1800-2.

Wu, D., C. Wang, and G. He, 2016: Gravity wave characteristics in two summer heavy rainfall in the Qinghai-Xizang Plateau. *Plateau Meteor.*, **35**, 854–864.

Wu, G., and Y. Zhang, 1998: Tibetan Plateau forcing and the timing of the monsoon onset over South Asia and the South China Sea. *Mon. Wea. Rev.*, **126**, 913–927, https://doi.org/10.1175/1520-0493(1998)126<0913:TPFATT>2.0.CO;2.

Xu, X., 2001: Synthetic physical image of the dynamic and thermal structure of Tibetan Plateau land-air processes. *Sci. China*, **31D**, 429–440.

——, T. Zhao, X. Shi, and C. Lu, 2015: A study of the Tibetan Plateau's thermal forcing in modulating rainband and moisture

transport in eastern China. *Acta Meteor. Sin.*, **73**, 20–35, https://doi.org/10.11676/qxxb2014.051.

Yanai, M., C. Li, and Z. Song, 1992: Seasonal heating of the Tibetan Plateau and its effects on the evolution of the Asian summer monsoon. *J. Meteor. Soc. Japan*, **70**, 319–351, https://doi.org/10.2151/jmsj1965.70.1B_319.

Yang, K., T.-T. Hu, and C.-H. Wang, 2017: A numerical study on the relationship between the spring-winter snow cover anomalies over the northern and southern Tibetan Plateau and summer precipitation in East China. *Chin. J. Atmos. Sci.*, **41**, 345–356.

Ye, D., and Y. Gao, 1979: *The Meteorology of the Qinghai–Xizang (Tibet) Plateau* (in Chinese). Science Press, 278 pp.

Zhang, J., B. Zhu, and F. Zhu, 1998: *Advances in Tibetan Plateau Meteorology* (in Chinese). Science Press, 268 pp.

Zhang, J.-P., S.-M. Fu, J.-H. Sun, X.-Y. Shen, and Y.-C. Zhang, 2015: A statistical and compositional study on the two types of mesoscale vortices over the Yangtze River basin. *Climatic Environ. Res.*, **20**, 319–336, https://doi.org/10.3878/j.issn.1006-9585.2015.14164.

Zhao, P., and Coauthors, 2018: The third atmospheric scientific experiment for understanding the Earth–atmosphere coupled system over the Tibetan Plateau and its effects. *Bull. Amer. Meteor. Soc.*, **99**, 757–776, https://doi.org/10.1175/BAMS-D-16-0050.1.

Zhao, S.-X., and S.-M. Fu, 2007: An analysis on the southwest vortex and its environment fields during heavy rainfall in eastern Sichuan Province and Chongqing in September 2004. *Chin. J. Atmos. Sci.*, **31**, 1059–1075.

——, and Coauthors, 2004: *Study on Mechanism of Formation and Development of Heavy Rainfalls on Meiyu Front in Yangtze River*. China Meteorological Press, 282 pp.

Zhao, Y., and Y. Wang, 2010: The dynamic diagnosis of eastward-moving characteristics and developing mechanism of two Tibetan Plateau vortex processes. *Plateau Meteor.*, **29**, 819–831.

Zheng, L.-L., J.-H. Sun, X.-L. Zhang, and C.-H. Liu, 2013: Organizational modes of mesoscale convective systems over central east China. *Wea. Forecasting*, **28**, 1081–1098, https://doi.org/10.1175/WAF-D-12-00088.1.

Zheng, Y., J. Chen, and P. Jun, 2008: Distribution and diurnal variation characteristics of mesoscale convective system in china and its surrounding areas in summer. *Chin. Sci. Bull.*, **4**, 471–481.